

Modeling of the Urban Heat Island on local climatic zones of a city using Sentinel 3 images: Urban determining factors

David Hidalgo García ^{*}, Julián Arco Díaz

School of Building Engineering, University of Granada, Spain



ARTICLE INFO

Keywords:

Urban Heat Island
Land surface temperature
Sentinel 3
Panel data model
Local climate zones and urban climate

ABSTRACT

Understanding how the components of cities interfere in the Urban Heat Island (UHI) has become a main great challenge for societies seeking to improve the quality of life through the implementation of urban planning criteria. In this research, the city of Granada (Spain) was divided into four local climatic zones (LCZ) according to the Corine Land Cover inventory, to study the land surface temperature (LST) and daytime and nighttime UHI using Sentinel 3 imaging. For each LCZ, urban factors were quantified by means of the Data Panel statistical analysis method, and multivariate relationships that statistically influence the UHI were determined. The results indicate an urban cooling island during the morning with a medium temperature of -0.6 K, the effect being greater in the low-density LCZ than in the high-density LCZ. At night, an UHI with an average temperature of 0.7 K is produced, this effect being greater in compact LCZs than in open ones. Two common factors significantly influence the day and night UHI: Fraction vegetation cover and solar radiation. In addition, for the day UHI, altitude and population density stand out as significant. For the night UHI, wind, impervious surface fraction factor and sky view factor additionally stand out.

1. Introduction

In recent decades, global warming and extreme weather events have become one of the most important and urgent challenges facing humanity (Kovats et al., 2005; Song et al., 2020). One process contributing very heavily to climate change is the modification of landscapes through the expansion of urbanized areas, motivated by high population growth (Li et al., 2011). According to a recent United Nations report, some 50% of the current population is urban, and the forecast is that the figure will increase to 70% by the year 2050 (ONU, 2018). These data translate as 2.5 billion additional urban dwellers in the next 30 years (Mukherjee and Singh, 2020), meaning a global increase in urban coverage amounting to approximately 1,527,000 km² (Schneider et al., 2010).

Urbanization drives the expansion of industry, transportation, and economic and urban growth, but it also alters the local urban climate by increasing the Land Surface Temperature (LST) (Scolozzi and Geneletti, 2012; Song et al., 2020). In recent years, numerous studies have underlined the positive correlation between LST and urban areas, which show higher temperatures than green areas or rural areas (Tsou et al., 2017; Karakuş, 2019; Hua et al., 2020; Yang et al., 2020a). Major increases in temperature can be traced to the phenomenon of urban climate alteration called Urban Heat Island (UHI), whose intensity is tied to multiple human activities (Santamouris, 2020). Recent studies indicate that cities with over one million inhabitants may have average annual temperatures 1 to 3 K higher than the surrounding non-urban areas (Khamchiangta and Dhakal, 2019).

* Corresponding author at: School of Building Engineering, University of Granada, Fuentenueva Campus, 18071 Granada, Spain.
E-mail addresses: dhidalgo@ugr.es (D. Hidalgo García), juliamn@ugr.es (J. Arco Díaz).

The UHI generates a series of environmental, climatic and socioeconomic problems that affect the quality of life in urban areas (Rozos et al., 2013; Yue, 2013; Dwivedi and Mohan, 2018; Macintyre et al., 2018; Yang et al., 2020a): the degradation of water and air quality (Feizizadeh and Blaschke, 2013), the reduction of biodiversity (Čeplová et al., 2017), changes in the energy balance (Arnfield, 2003), detrimental effects on the regional climate (Sarrat et al., 2006), an increased cost of energy (Santamouris, 2020), and even increased mortality (Arbuthnott and Hajat, 2017). Because these are growing problems for urban populations, exhaustive knowledge of the properties involved and the factors that intensify them is crucial to establish adequate urban planning measures for mitigating their end effects.

Among the different methodologies that can be used to determine this phenomenon, remote sensing should be highlighted. It lends the possibility of carrying out large-scale urban LST and UHI studies (Song et al., 2018) using satellite images with Thermal Infrared Sensors (TIRS). Such studies conform an important and extensive field of research (Wang and Ouyang, 2017; Yao et al., 2018; Sejati et al., 2019; Guo et al., 2020; Hu et al., 2020; Roy et al., 2020; Shafizadeh et al., 2020; Yang et al., 2020a, 2020b).

Landsat 8 satellite images launched into orbit in 2013 allow for LST estimates every 16 days at a resolution of 100 m, thanks to the thermal infrared sensor bands 10 and 11. This system has been used to determine the UHI of Bangladesh (Roy et al., 2020), Changchun (China) (Yang et al., 2020a), Barcelona, (Spain) (Lemus et al., 2020), Shanghai (China) (Li et al., 2011), the Olympic area of Beijing (China) (Hu et al., 2020), Xiamen city (China) (Hua et al., 2020), the Mediterranean region (Jato, 2019), Fuzhou (China) (Du et al., 2020), Lyon (France) (Diallo et al., 2015) or Krakow (Poland) (Walawender et al., 2014). An older but highly accurate product is Sentinel 3, offering 3A, 3B and 3C imaging. The first two satellites were launched in February 2016 and April 2018, respectively, while the Sentinel 3C does not yet have a launch date. All Sentinels have three TIRS channels—bands 7, 8 and 9—that provide LST estimates every 27 days and at a resolution of 1000 m.

Similar studies carried out on the cities of Londrina, Brazil (Anjos et al., 2020), Glasgow (Emmanuel and Krüger, 2012), Bangkok (Khamchiangta and Dhakal, 2019) or the Beijing Olympic area (Hu et al., 2020) report higher intensities for night UHI, the warmest areas being in central areas of the cities as opposed to the suburban or rural areas. The methodology used to obtain the temperatures in the Glasgow study entailed comparing environmental temperatures—rural versus urban—with reference to meteorological stations. In the remaining studies, Landsat 8 satellite images and split window (SW) algorithms were used to obtain the LST and proceed to study the UHI.

The city under study presents important problems related to the local climate, very much conditioned by the proximity of the Sierra Nevada mountain range (30 km) and of the Sea (60 km). Granada is located in the Mediterranean Sea basin, and is held to be highly vulnerable to climate change given its rising temperatures when compared to the rest of the planet (Ward et al., 2016; Cramer et al., 2018). In addition to these geographic and climatological factors, Granada has become in recent years the third most environmentally polluted city in Spain. To the best of our knowledge, this is the first study dedicated to LST and UHI estimates using satellite images of the study area, and one of the first conducted on a Spanish city, after the studies of Barcelona (Arellano et al., 2018; Lemus et al., 2020) and Madrid (Rasilla et al., 2019).

Numerous authors have investigated the spatial-temporal variability of UHI in urban areas using satellite images. Some studies did not take into account the environmental conditions or the physical structure of cities (Emmanuel and Krüger, 2012; Carvalho et al., 2017; Anjos et al., 2020), while others focused on a single factor (Feizizadeh and Blaschke, 2013; Tan and Li, 2015; Barbieri et al., 2018) or just a few (Dai et al., 2018; Khamchiangta and Dhakal, 2019). Paradoxically, and although numerous studies positively link environmental pollution with an increase in LST and UHI intensities in urban areas (Li et al., 2011; Schwarz et al., 2011; Logan et al., 2020; Venter et al., 2020), their potential impact on the precision of Sentinel LST values has not been studied to date. The geographical and climatic conditions, together with the high pollution of the city of Granada, make it an ideal site for such research. Our work includes determination of the LST and UHI through satellite images and their relationships with 13 physical and/or environmental factors that are then statistically analyzed in order to determine the strength of the correlations, so as to identify the main causes of the city's warming. It is a thorough study that provides for a comprehensive understanding of the UHI and the factors that influence each LCZ in the city of Granada; and our results may be extrapolated to any other city of similar characteristics.

The methodology most often used in LST studies entails Landsat images rather than Sentinel images. Yet the fact that Landsat passes over each point on the planet just once every 16 days must be seen as a significant inconvenience—it only allows for determination of the particular LST and UHI at that specific time interval. Existing studies tend to extrapolate such point values to global periods in order to arrive at total results. This is an erroneous premise, since recent research (Emmanuel and Krüger, 2012; Anjos et al., 2020) warns of the high variability of the UHI throughout the day and over time. In this research, the use of the statistical method called Data Panel is presented as a novel element with respect to the methods usually used in research on UHI existing in the literature. The main statistical approaches and methods commonly used are: descriptive statistics of linear correlations and regressions (Li et al., 2011; Khamchiangta and Dhakal, 2019; Song et al., 2020; Yang et al., 2020), Multiple Regression Analysis (MRA) (Wang and Ouyang, 2017; Jato, 2019; Straub et al., 2019), Bivariate correlation (Soydan, 2020) or ANOVA (Connors and Galletti, 2013; Li et al., 2015; Masoudi et al., 2021). The Data Panel method, in comparison with the above methods, allows for the incorporation of more data and variables, since it admits the inclusion of the individual effects of a certain area or neighborhood to obtain the global results. It also permits inclusion of the spatial residual values of the results, eliminating the usual problem of collinearity between variables. Such considerations are often neglected by traditional methods; yet they provide for more accurate and complete results.

Therefore, the questions that we propose to answer with this research are the following: 1. Can Sentinel 3 obtain adequate LST values to be used in UHI studies in a city with climatic and pollution conditions such as Granada? 2. What influence does each factor analyzed have on the day and night UHI of the city? 3. How do the impacts of the factors analyzed vary in each LCZ of the day and night UHI? 4. Can the results obtained prove important for future urban planning?

The most novel aspect of this research is that the methodology put forth here to determine the UHI under an open-source

environment lends more or less equal weight to the LCZ classification, the LST determination, and some specific physical and environmental factors that apply to the city of Granada. This combination of factors allows UHI variations to be monitored urgently, accurately and economically. Moreover, the fact that Sentinel 3 thermal images are of free and open access, recording physical, environmental and climatic variables (including the LST) from any point of the planet since it was put into orbit, permits a broader realm of extrapolation and interpretation of our findings. The geographic, climatological and pollution characteristics of our city contribute to the empirical evidence obtained in previous UHI studies. Such considerations could mean enhanced decision-making by urban planners and public administrations, so that future growth zones of cities elsewhere would include mitigation measures for UHI-related effects.

2. Materials and methods

2.1. Study area and data source

The area under study is the municipality of Granada, in Andalusia, southern Spain. The UTM geographic coordinates of the city are: latitude 37.111741 N and longitude 03.362401 W; its altitude is 680 m above sea level (Fig. 1).

It has a population of 232,462 and covers an area of 880,000 km². Its climate is strongly conditioned by its location at the foothills of Sierra Nevada, a mountain range with an average altitude of 2045 m, reaching a maximum of 3482 m above sea level at Mulhacen peak. This is the highest mountain massif in Western Europe after the Alps. However, Granada is also just 60 km north of the Mediterranean coast. According to the Koppen-Geiger climate classification, it has a transitional climate between the Mediterranean climate (Csa) and the cold semi-arid climate (Bsk), which implies humid and mild winters and hot and dry summers (De Castro et al., 2007). The average temperature fluctuates between 279.65 K for the month of January and 298.45 K for the month of July, with minima in winter of 270.15 K and summer extremes of 316.15 K. The approximate number of hours of sunshine per year is 2917, giving an average of 7.99 h of sunshine per day.

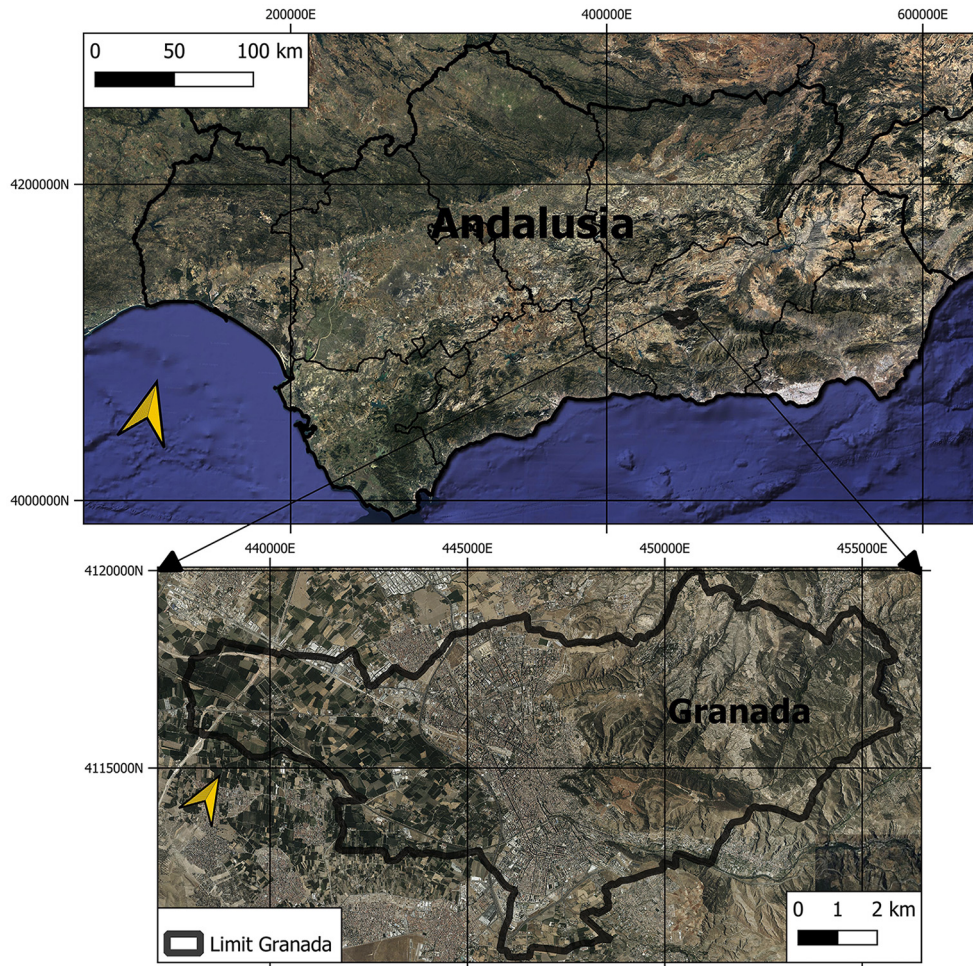


Fig. 1. Study area of Granada, Andalusia, Spain. Image source: Google earth.

2.2. Sentinel 3 images

Sentinel 3 satellites are equipped with the high-resolution scanning instrument Land Surface Temperature Radiometer, enabling LSTs of the Earth's surface to be obtained. The images consist of six spectral bands with a resolution of 500 m (bands S1 to S6) and three thermal bands that make it possible to determine the LST (bands S7, S8 and S9) with a spectral resolution of 1000 m. These three TIRS bands operate with wavelength ranges of 3.7, 10.85, and 12 μm , respectively. The S8 and S9 bands present spectral responses similar to the 11 μm and 12 μm channels of the predecessors ENVISAT ATSR and NOAA AVHRR Terra / Aqua MODIS, permitting the use of split window algorithms to calculate the LST. The Sentinel 3 SLSTR sensor provides for slightly higher pixel counts than MODIS due to an improved detection threshold and somewhat greater sensitivity (Wooster et al., 2012). In similar investigations (Freeborn et al., 2009; Wooster et al., 2012; Xu et al., 2020), 90% of the pixels of MODIS and Sentinel 3 are found to coincide, with a 10% commission error in the MODIS product. In turn, Sentinel 3 identifies 44% more pixels than MODIS where nothing is detected. The use of Sentinel 3 was therefore considered more appropriate than MODIS for our research, involving a medium-sized city.

Sentinel 3 thermal products have three levels of processing (level 0, level 1 and level 2), although only the last two are available for download. Those of level 1 present radiance and brightness temperatures that require split window (SW) algorithms to obtain the LST. Level 2 products directly and automatically include the LST along with associated parameters such as the NDVI, PV and NDBI.

The city of Granada is located under the route of the Sentinel 3A and 3B satellites. The usual time of passage of 3A over the city is between 10:00 and 11:00 a.m. 3B passes over Granada between 20:00 and 21:00 h, that is, 8:00 to 9:00 p.m. The images chosen for the study correspond to twelve days distributed as evenly as possible over the months from November 2018 to October 2019. Throughout this time interval, a total of 24 images were used, 12 corresponding to the Sentinel 3A (Table 1) and 12 to Sentinel 3B (Table 2). From here on, the first (Sentinel 3A) will be identified as Sentinel day and the second (Sentinel 3B) as Sentinel night. All of them have a cloudiness index of less than 15% in order to ensure accuracy in obtaining the LST and subsequently calculating the UHI. The images used were acquired through the European Space Agency (ESA) Copernicus Open Access Hub for level 2.

After downloading the images, the spatial resolutions of bands 8 and 9 were reclassified to a spectral resolution of 100 m, and georeferenced using the ETRS89 / UTM Zone 30 N projection system. Both the reclassification and the atmospheric correction in OLI bands were carried out using the Toolbox (S3TBX) under the open-source software environment Sentinel Application Platform (SNAP), version 7.0.0.

2.3. On-site LST determination and validation

For this research, the calculation of the LST was carried out in situ by collecting data with high-precision temperature and humidity dataloggers. Eighteen probes (Testo brand, model 184H) homologated and with a calibration certificate were placed around the city (Srivastava et al., 2009; Li and Meng, 2018; Meng et al., 2019; Sekertekin, 2019; Wang et al., 2019; Yang et al., 2020a, 2020b). Fig. 3 shows the locations chosen for these monitoring probes. Table 3 shows the location, elevation, ground cover and area data for each probe installed in the city.

The dataloggers used have operating temperatures ranging between 253.15 and 343.15 K, with an accuracy of ± 0.5 K (273.15–343.15 K) and ± 0.8 K (253.15–273.15 K) and a resolution of 0.1 K. With regard to humidity, the accuracy is $\pm 2\%$ at +298.15 K, (20% to 80% RH) and $\pm 3\%$ at +298.15 K (<20% and > 80% RH). They were programmed to record the temperature and humidity values in a 15-min interval during the entire period of time that the study lasted. A total of 175,200 temperature data and just as many humidity data were gathered.

2.4. Methodology

The methodology applied in this research study is described in Fig. 2.

The city was broken down into six different local climatic zones (LCZ)—Compact vs Open High-Rise, Compact vs Open Low-Rise, Scattered Trees and Low Plants—as an approach to characterize the landscape and the urban structure. In this way, we could precisely

Table 1

Sentinel 3A images used, acquired from the Copernicus Open Access Hub service.

Number	Date (yyyymmdd)	UTC Time (hhmm)	Cloudiness	Sentinel 3A file name
1	20181129	10:15	0	S3A_SL_2_LST__20181129T101505_LN2_003.SEN3
2	20181215	10:22	5	S3A_SL_2_LST__20181215T102215_LN2_003.SEN3
3	20181231	10:08	6	S3A_SL_2_LST__20181231T100824_LN2_003.SEN3
4	20190217	10:43	11	S3A_SL_2_LST__20190217T104324_LN2_003.SEN3
5	20190321	10:13	6	S3A_SL_2_LST__20190321T101328_LN2_003.SEN3
6	20190501	10:20	12	S3A_SL_2_LST__20190501T102045_LN2_003.SEN3
7	20190625	10:24	0	S3A_SL_2_LST__20190625T102447_LN2_003.SEN3
8	20190711	10:09	1	S3A_SL_2_LST__20190711T100949_LN2_003.SEN3
9	20190727	10:26	13	S3A_SL_2_LST__20190727T095451_LN2_003.SEN3
10	20190828	11:05	5	S3A_SL_2_LST__20190828T110550_LN2_003.SEN3
11	20190929	10:35	3	S3A_SL_2_LST__20190929T103559_LN2_003.SEN3
12	20191015	10:21	1	S3A_SL_2_LST__20191015T102102_LN2_003.SEN3

Table 2

Entinel 3B images used, acquired from the Copernicus Open Access Hub service.

Número	Date (yyyymmdd)	UTC Time (hhmm)	Cloudiness	Sentinel 3B file name
1	20181129	20:25	0	S3B_SL_2_LST__20181129T202515_LN2_003.SEN3
2	20181215	20:32	5	S3B_SL_2_LST__20181215T203245_LN2_003.SEN3
3	20181231	20:18	6	S3B_SL_2_LST__20181231T201814_LN2_003.SEN3
4	20190217	20:43	11	S3B_SL_2_LST__20190217T204354_LN2_003.SEN3
5	20190321	20:22	6	S3B_SL_2_LST__20190321T202208_LN2_003.SEN3
6	20190501	20:25	12	S3B_SL_2_LST__20190501T202533_LN2_003.SEN3
7	20190625	20:27	0	S3B_SL_2_LST__20190625T202717_LN2_003.SEN3
8	20190711	20:19	1	S3B_SL_2_LST__20190711T201909_LN2_003.SEN3
9	20190727	20:36	13	S3B_SL_2_LST__20190727T203631_LN2_003.SEN3
10	20190828	21:15	5	S3B_SL_2_LST__20190828T211555_LN2_003.SEN3
11	20190929	20:45	3	S3B_SL_2_LST__20190929T204505_LN2_003.SEN3
12	20191015	20:11	1	S3B_SL_2_LST__20191015T201102_LN2_003.SEN3

Table 3

Location and characteristics of the control points.

Site	Lat/Lon	Elevation (m)	Land Cover	Zone	Surface characteristics
1	37.156005 N/ -3.587614 W	691.53	Buildings	Industrial	2
2	37.178882 N/ -3.593339 W	698.44	Buildings	Periphery	4
3	37.198047 N/ -3.628600 W	656.73	Buildings	Downtown	3
4	37.181357 N/ -3.606877 W	669.32	Buildings	Downtown	2
5	37.172864 N/ -3.608857 W	662.46	Green Space	Periphery	2
6	37.191195 N/ -3.639708 W	629.80	Buildings	Downtown	1
7	37.204308 N/ -3.616840 W	693.84	Green Space	Downtown	2
8	37.198052 N/ -3.610125 W	696.70	Buildings	Downtown	1
9	37.190676 N/ -3.623962 W	660.96	Buildings	Downtown	2
10	37.192251 N/ -3.594950 W	779.97	Buildings	Periphery	2
11	37.175192 N/ -3.599760 W	680.30	Low Plants	Rural Zone	6
12	37.168874 N/ -3.596016 W	668.68	Scattered Trees	Rural Zone	5
13	37.166492 N/ -3.605211 W	661.63	Low Plants	Rural Zone	6
14	37.160306 N/ -3.599876 W	670.63	Buildings	Periphery	3
15	37.154731 N/ -3.601885 W	670.78	Green Space	Downtown	2
16	37.196394 N/ -3.674166 W	597.90	Buildings	Downtown	2
17	37.181457 N/ -3.568955 W	761.05	Buildings	Downtown	1
18	37.189862 N/ -3.789886 W	562.21	Buildings	Periphery	1

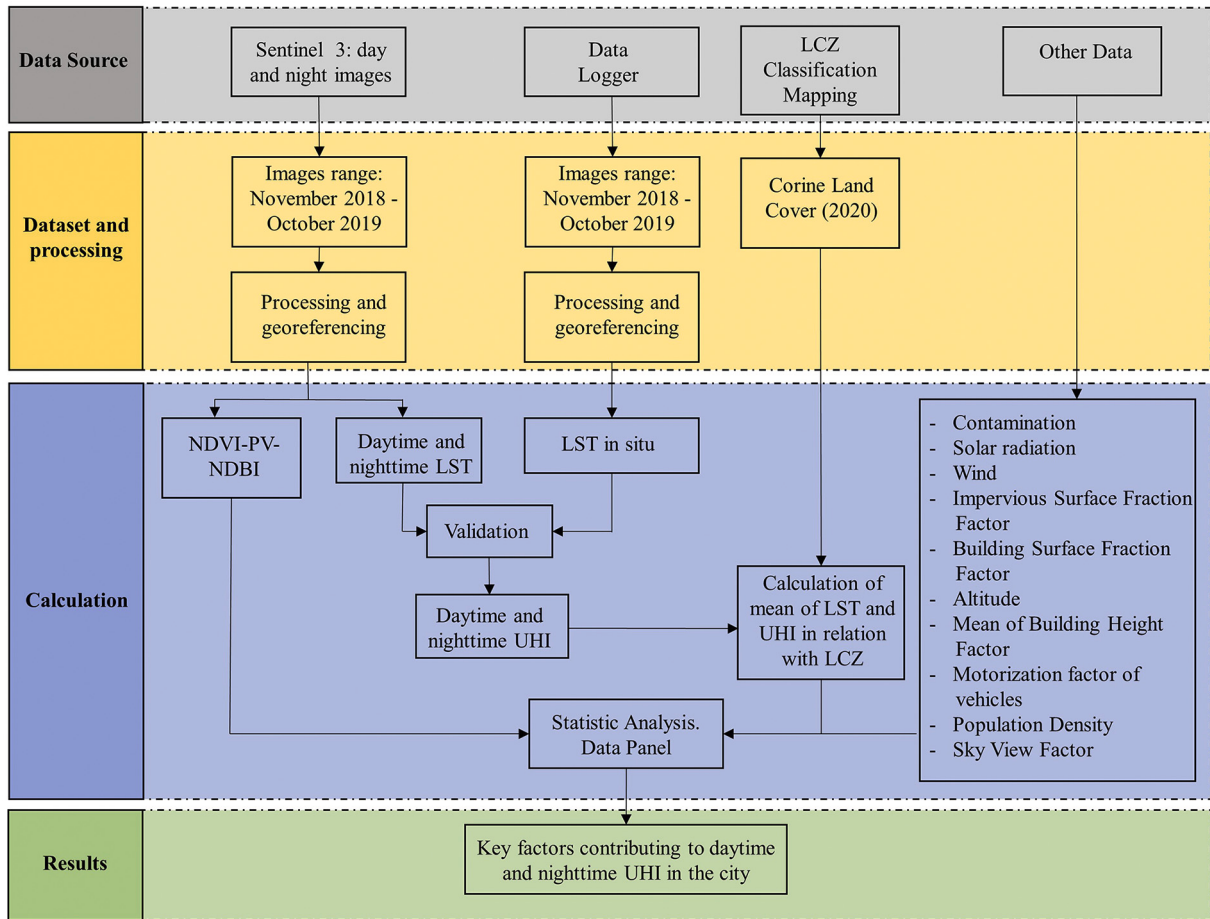
Note: Surface Characteristics: 1: Few or no trees. Land cover paved: Concrete, steel, and stone. 2: Few or no trees. Land cover paved: Brick, tile, and concrete. 3: Land cover paved but with scattered trees: Concrete, steel, stone, and glass. 4: Land cover paved but with scattered trees: Wood, brick, tile, and concrete. 5: Natural forest. Land cover pervious. 6: Few or no trees. Natural grassland or agriculture.

identify the factors that have a greater or lesser impact on each LCZ. A number of factors were established: Normalized Difference Vegetation Index (NDVI), Fraction Vegetation Cover (PV), Normalized Difference Built-Up (NDBI), Mean of Building Height Factor, Fraction of Building Facades, SVF and Impervious Surface Fraction Factor (ISA), Pollution, Number of Vehicles as a Factor, Solar Radiation, Wind, Altitude and Population Density. Then the correlation between the data obtained and the relationship between the dependent variable and the independent variables of each LCZ was determined by statistical analysis using the Panel Data method.

This method allows statistical analysis of multivariate time series including the individual effects of each individual. This circumstance, compared to other traditional methods of analysis, allows the results obtained to include a greater number of data, eliminating the usual problem of collinearity between variables. The use of this method in our research allowed us to reflect the possible variations of the conditions of each LCZ contemplated in the final results, which makes it a unique and powerful approach. It is validated by other investigations (Chen et al., 2011; Alcock et al., 2015; Fang and Tian, 2020) similar to ours, which includes time series with multiple LCZs and quantitative variables that might change the conditions of the LCZ analyzed. This is a particularly appropriate approach to assess the UHI in a medium-sized city featuring high thermal contrast and high pollution (as is the case of Granada), as it allows one to obtain both the daytime and the nighttime UHI in view of the physical and environmental characteristics of each LCZ.

2.5. Local climate zone classification mapping

Our study is based on the Local Climate Zones (LCZ) classification proposed by the authors Stewart and Oke (2009). These are regions of uniform coverage, structure, and human activity that span a variable surface area. Therefore, each presents a specific temperature regime —given its properties (Stewart and Oke, 2012)— that persists over time, being associated with the homogeneous environments and ecosystems of cities. LCZs are acknowledged in the literature as very relevant for characterizing land cover by satellite images (Stewart, 2011; Qiu et al., 2018). Their utility in UHI studies is widely documented (Emmanuel and Krüger, 2012;

**Fig. 2.** Methodology.

(Wang and Ouyang, 2017; Brousse et al., 2019; Khamchiangta and Dhakal, 2019; Anjos et al., 2020; Equere et al., 2020). The objectives of using this classification in our research are: to characterize the landscape of the city of Granada through a global and commonly used system, and to extrapolate the LST and UHI data obtained for each LCZ to any other city. The use of LCZ to describe factors affecting UHI is particularly attractive for cities that did not undergo planned development (Khamchiangta and Dhakal, 2019; Anjos et al., 2020; Oliveira et al., 2020), as is the case of Granada.

The process carried out to derive the LCZ map of Granada is described below. Based on the Corine Land Cover (CLC) inventory for the year 2020 and following the LCZ selection models and criteria established by Stewart and Oke (2009), the city was divided into six LCZs: Compact High-Rise, Compact Low-Rise, Open High-Rise, Open Low-Rise, Scattered Trees, and Low Plants. The classification and definitions of the six zones are presented in Fig. 3 and Table 4.

The different urban/architectural structures of the city and its coverage (green or other) were taken into account, which led us to coherent and homogeneous references for the chosen LCZ system. The methodological steps established to choose the LCZ were: (1) Collection of city metadata based on the CLC and real high-resolution images from Google Street View (Yang et al., 2019) and Sentinel 2 satellites. (2) Definition of the thermal source area in view of orientation parameters, solar radiation, climatology and wind. (3) Visual comparison of the LCZ map of the CLC with the high-resolution images. (4) Selection and delimitation of LCZs. According to the data obtained in points 1, 2 and 3, the LCZs were catalogued, also taking into account the coincidence, not necessarily exact, of the sites with the LCZ classes. The mean values of the properties of each LCZ were found to be within the ranges of standard values established by Stewart and Oke (2009).

A qualitative and quantitative comparison of land cover —impermeable, permeable and natural surfaces— according to the Corine Land Cover inventory with updated coverage from Google Street View (Yang et al., 2019) and Sentinel 2 satellite images showed that only two of the 18 reference points did not coincide with the CLC inventory. This means a 95% match with the CLC inventory, applied to the appropriate coverage corrections and included in the corresponding LCZ. We then proceeded to visit the LCZs defined in this research to corroborate in situ coincidence with the images and the mean LCZ characteristics established by Stewart and Oke (2012). In general, the LCZs of our research match the satellite images and Google Street View, presenting values within the limits set forth by the cited authors.

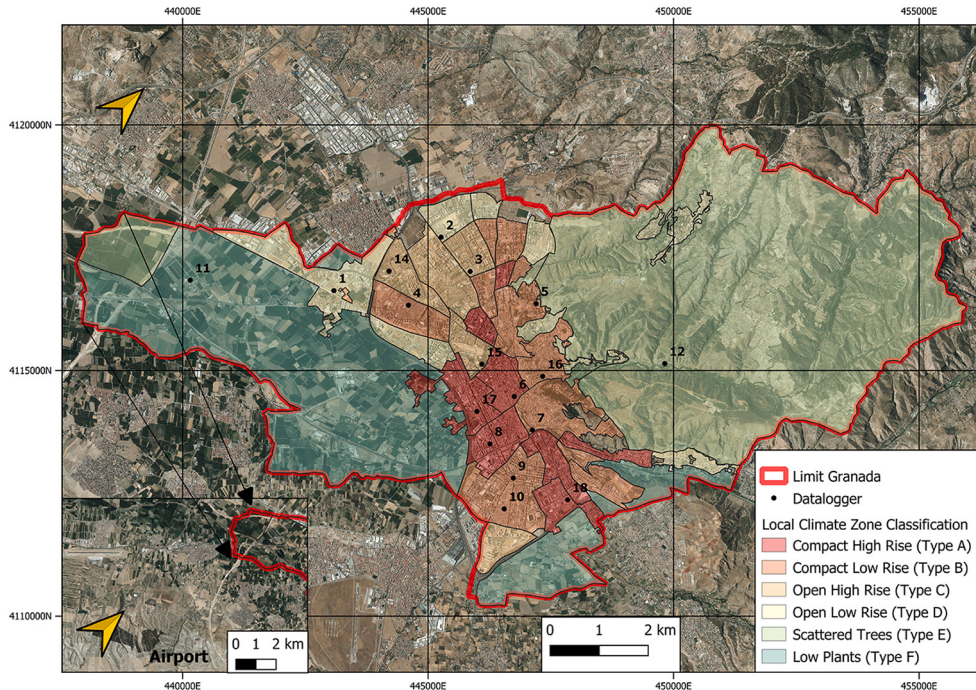


Fig. 3. Local Climate Zone Classification Mapping and Location of monitoring points. Image source: The National Geographic Institute (Spain's Ministry of Transport).

2.6. Land surface temperature estimation

The existing SW algorithms to gauge LST are based on the concept of differential absorption (McMillin, 1975), whereby the difference between the two TIRS band wavelengths allows for correcting for the atmospheric effects produced on the signal. It is also possible to do this using a TIRS band at two different wavelengths, or a TIRS band at two different viewing angles. They depend on the emissivity of the earth's surface, which can be obtained in multiple ways (Ruescas et al., 2016). Abundant studies report on the validation, use and precision of these algorithms in Sentinel 3 images (Coppo et al., 2010; Wan, 2013; Ruescas et al., 2016; Sobrino et al., 2016; Prikaziuk and Van der Tol, 2019; Chiang, 2020; Yang et al., 2020a, 2020b).

The SW algorithm of the official Sentinel level 2 SLSTR product implicitly incorporates soil emissivity by means of the following equation (Remedios, 2012):

$$LST = a_{f,i,pw} + b_{f,i} \left(T_{11} - T_{12} \right)^{\frac{1}{\cos(\theta)}} + (b_{f,i} + c_{f,i}) T_{12} \quad (1)$$

where LST is the surface temperature in K, a, b and c are coefficients dependent on the vegetation cover and the biome, and T11 and T12 are the brightness temperatures of bands 8 and 9 of Sentinel 3, respectively. θ is the zenith angle of view of the satellite and m is a dependent variable of θ (Remedios, 2012; Yang et al., 2020a, 2020b).

2.7. Urban Heat Island estimation

According to the existing literature on the phenomenon, UHI is defined as the difference in temperatures between measurements within the urban area and rural areas surrounding the city, taken at the same time (Oke, 1987). Therefore, the UHI can be determined according to eq. 2:

$$UHII = Turban - Trural \quad (2)$$

In order to obtain rural temperatures, the Meteorological Station (pertaining to the Spanish Meteorological Agency, AEMET) located at the Granada airport was selected. Its UTM coordinates are: 37.189667 N and – 3.7894250. The station is located 16 km from the city center, at an altitude of 657 m. It is seen in Fig. 2 as point 13. Its validity as a reference point for taking rural temperatures depends on the following considerations (Wang et al., 2017): 1) The % of impervious surfaces around the station is 10%, that being the % of farmland from 1990. 2) The difference in surface elevation between the station and the city of Granada is approximately 30 m. 3) The station (at a distance of 16 km) lies clearly outside the urban area. These conditions make it a suitable rural temperature point for such studies, following Wang et al. (2017). With the LST images of Sentinel day and night exported to the QGIS software, version

Table 4

Building types and zones.

Built Types	Definition	Built Types	Definition
a) Compact High Rise		Dense mix of tall buildings to tens of stories. Few or no trees. Land cover mostly paved. Concrete, steel, stone, and glass construction materials.	b) Compact Low Rise
			Dense mix of low-rise buildings (1–3 stories). Few or no trees. Land cover mostly paved. Stone, brick, tile, and concrete construction materials.
c) Open High Rise		Open arrangement of tall buildings to tens of stories. Abundance of pervious land cover (low plants, scattered trees). Concrete, steel, stone, and glass construction materials.	d) Open Low Rise
			Open arrangement of low-rise buildings (1–3 stories). Abundance of pervious land cover (low plants, scattered trees). Wood, brick, stone, tile, and concrete construction materials.
e) Scattered Trees		Lightly wooded landscape of deciduous and/or evergreen trees. Land cover mostly pervious (low plants). Zone function is natural forest, tree cultivation, or urban park.	f) Low Plants
			Featureless landscape of grass or herbaceous plants/crops. Few or no trees. Zone function is natural grassland, agriculture, or urban park.

Images source: Google Earth.

3.10.5, and with the help of the raster calculator command, the UHI of the city was determined by means of eq. 2.

2.8. NDVI, PV and NDBI

Like the LST, the NDVI, PV and NDBI values were obtained using the calculation algorithms developed and applied by ESA on the official SLSTR level 2 products.

These were pre-processed using the SNAP Sentinel 3 toolbox and exported to QGIS software, version 3.10.5. (See Figs. 4–6

2.9. Other data

2.9.1. Contamination

The reference serving to calculate air quality was the Air Pollution Index (API), which is commonly used to measure air pollution (Bereitschaft and Debbage, 2013; Sun et al., 2016; Wang et al., 2017; Zhou et al., 2018). It takes the form of a non-dimensional number in the range of 0 to 500 and provides a generalized degree of air pollution and the accompanying health hazards. Its statistical characteristics are described in Table 3.

The API is an integrated measure that reflects the levels of three fundamental air pollutants: SO₂, NO₂ and PM10. Each is calculated individually, and the overall API of the city is derived from the highest API of these three air pollutants.

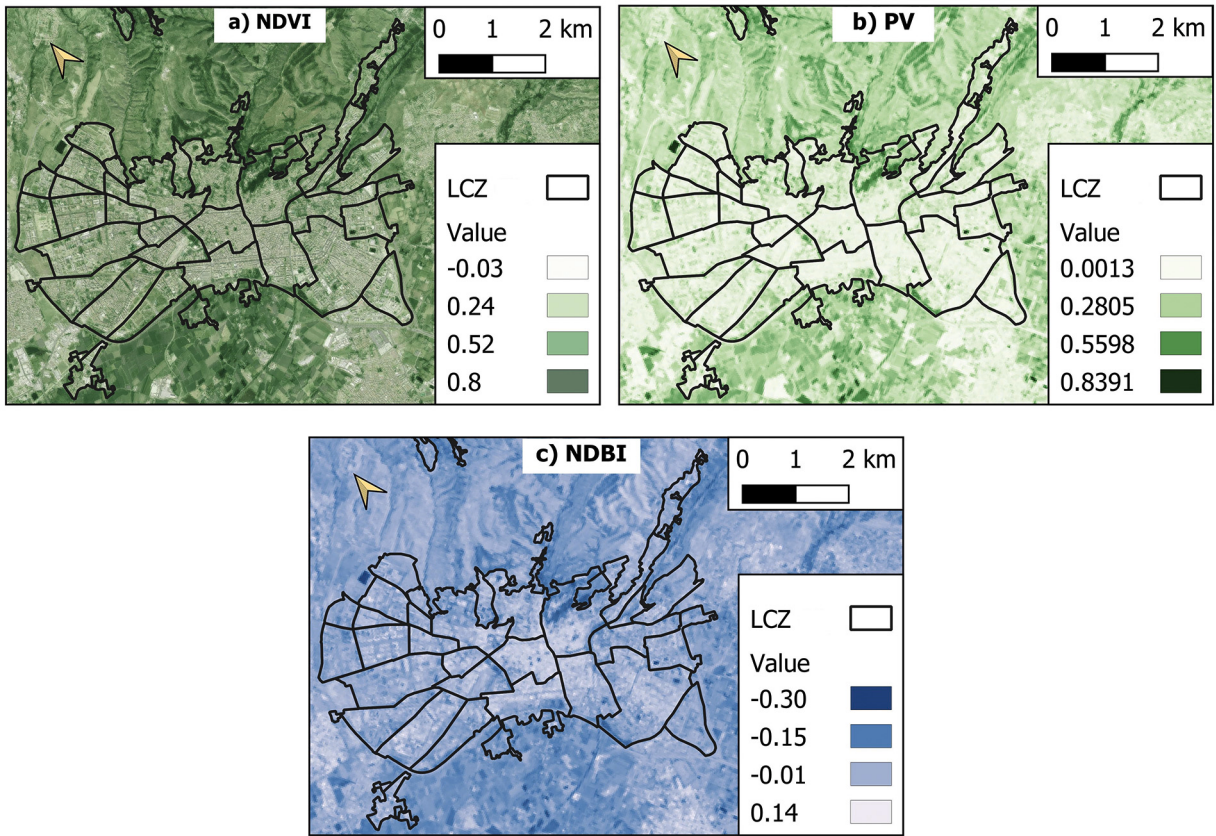


Fig. 4. Values: a) NDVI; b) PV and c) NDBI of the city of Granada. Image source: The National Geographic Institute (Spain's Ministry of Transport).

The interpolation to calculate the API of the city of Granada was performed using the following equation (Sun et al., 2016; Zhou et al., 2018):

$$API = \frac{(API_u - API_L)}{(C_u - C_l) x (C_i - C_l)} + API_{Li}, \quad (3)$$

where API is the index for pollutant i (the most substantial of the three pollutants SO_2 , NO_2 , and PM_{10}), C_i is the observed concentration of pollutant i , and C_u and C_l are the upper and lower limits of the range (shown in Table 5), within which the C_i , API_u and API_L are the upper and lower limits of the corresponding API interval (shown in Table 6). Finally, API_{Li} is the value of the lower range when moving to a higher range (Sun et al., 2016; Zhou et al., 2018).

2.9.2. Solar radiation

Solar radiation data for the LCZs were obtained through simulations with System for Automated Geoscientific Analyses (SAGA) software for QGIS (Conrad et al., 2015), which allows digital surface models to be imported thanks to the Light Detection And Ranging (LIDAR) program. SAGA was created in 2007 by researchers from the University of Hamburg (Germany). Its simulations of solar radiation of soils and cities are widely cited and validated in the literature (Zakšek et al., 2005; Olaya and Conrad, 2009; Bremer et al., 2016).

The AEMET meteorological station at Granada Airport (Fig. 3, point 13) is an approved and certified measurement point for direct and diffuse solar radiation. The former relies on a Kipp-Zonen Pyrheliometer; the latter on a Kipp-Zonen Pyranometer, periodically calibrated in view of international standards. After comparing the radiation data from the meteorological station to the data simulated by SAGA software, a precision error of 1% was detected in the mean values of radiation at the hours of passage of Sentinel day and night. This value is in line with those determined in other studies (Zakšek et al., 2005; Bremer et al., 2016) involving the simulation of solar radiation using SAGA software.

2.9.3. Wind

The wind is a key element affecting the UHI intensity in cities (Van Hove et al., 2015; Gaur et al., 2018). Wind speed and directional data were obtained from the Meteorological Station at Granada's airport (AEMET). Subsequently, using the SAGA software for QGIS, the value was simulated for the LCZ established within the city.

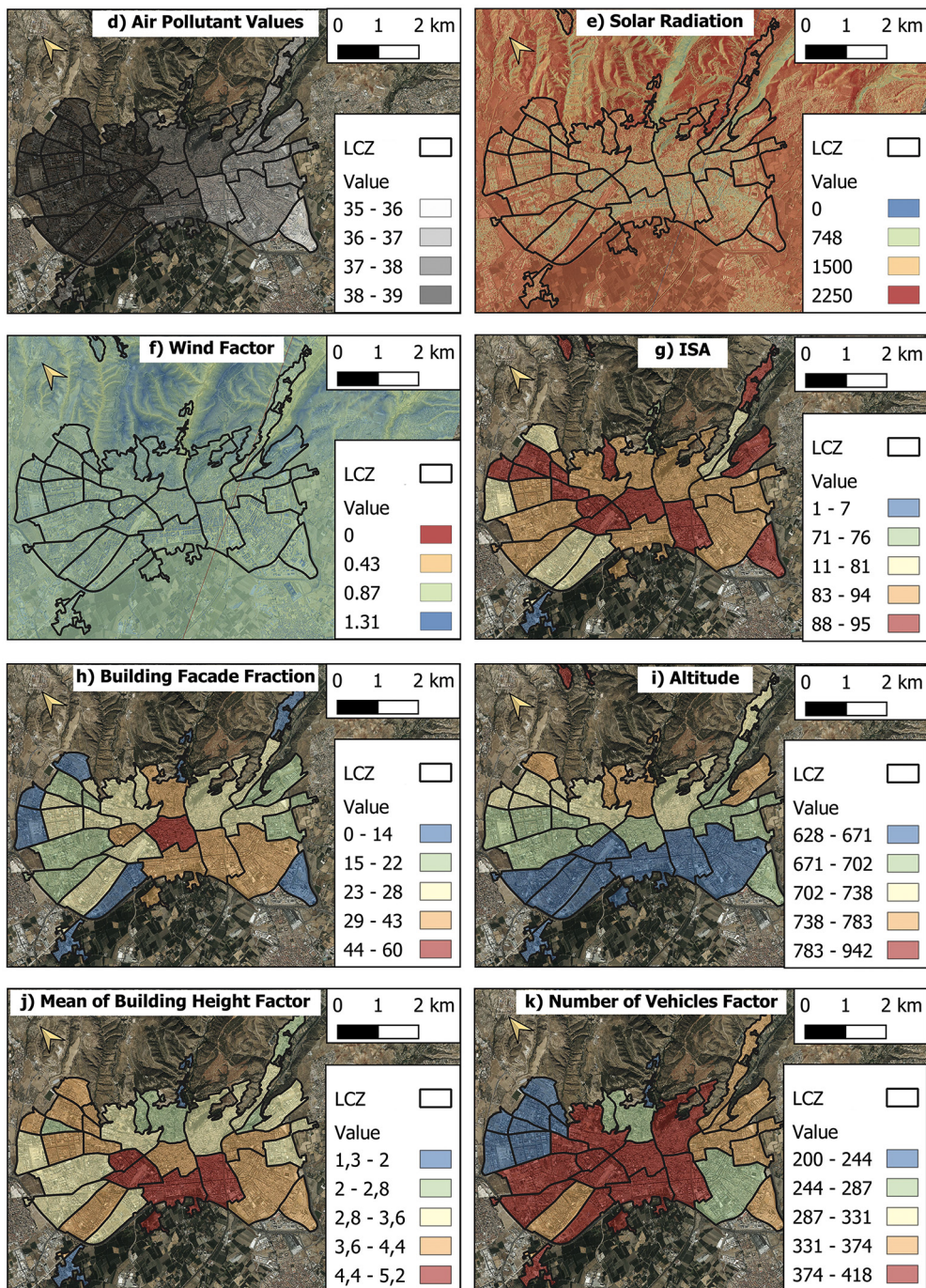


Fig. 5. Other factors: d) Air Pollutant values (API); e) Solar Radiation (KW/m^2); f) Wind Factor; g) ISA (%); h) Building Facade Fraction (5); i) Altitude (m asl); j) Mean of Building Height Factor (m) and k) Number of Vehicles Factor (number/1000 inhabitants). Image source: The National Geographic Institute (Spain's Ministry of Transport).

2.9.4. Impervious surface fraction factor

The impervious surface fraction refers to the proportion of the ground surface with an impervious covering such as asphalt, concrete, tile or ceramic pavements. This fraction represents the area of impervious surfaces divided by the total area of the LCZ, ranging from 0 to 100%. For its calculation, the data on impervious surfaces of the Geographic Information System (GIS) of the Electronic System of the Cadastre (under the Government of Spain) were taken into account.

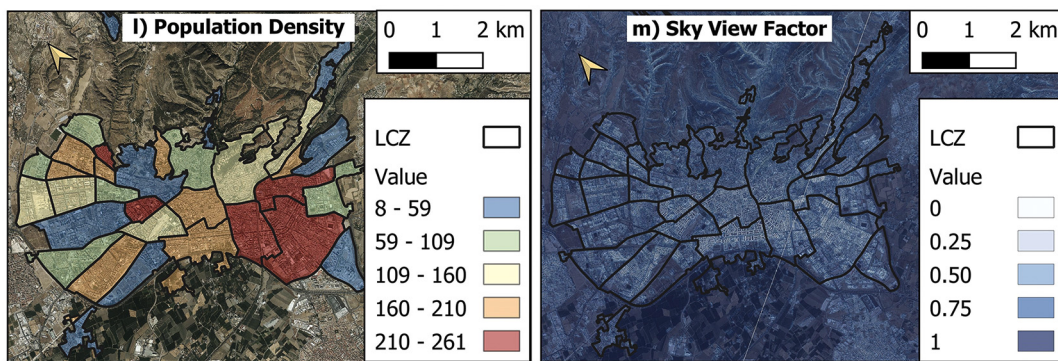


Fig. 6. Other factors II: i) Population Density (people/km²); m) Sky View Factor. Image source: The National Geographic Institute (Spain's Ministry of Transport).

Table 5

API limit values.

API	Air quality - class	Air quality - evaluation	Health effects
0–50	I	Excellent	Harmless
51–100	II	Good	Acceptable
101–200	III	Medium pollution	Sensitive
201–300	IV	Moderate pollution	Unhealthy
301–500	V	Severe pollution	Very unhealthy

Table 6

API concentration intervals.

API Intervals	SO ₂	NO ₂	PM ₁₀
0–50	0.000–0.050	0.000–0.080	0.000–0.050
51–100	0.050–0.150	0.080–0.120	0.050–0.150
101–200	0.150–0.800	0.120–0.280	0.150–0.350
201–300	0.800–1.600	0.280–0.565	0.350–0.420
301–500	1.600–2.620	0.565–0.940	0.420 – 0.600

2.9.5. Building facade fraction factor

The fraction of facade surfaces refers to the proportion of buildings' surfaces: walls and envelopes, including ceramic concrete faces, cladding and other materials. This factor represents the area of the facade surfaces divided by the total LCZ area, between 0 and 100%. For its calculation, the 2D data of the city's buildings from the Geographic Information System (GIS) of the Cadastre Electronic System were taken into account. With them, 3D modeling was performed using QGIS software to derive the total façade surfaces of the buildings.

2.9.6. Altitude

Altitude is known to affect urban climates, and should be accounted for when calculating the intensity of the UHI (Gaur et al., 2018). The average data for altitude of each LCZ were calculated with QGIS based on data from the Digital Terrain Model of Spain, with a mesh pitch of 2 m, downloaded from the National Geographic Institute (Spain's Ministry of Transport). The LCZ zones of the city of Granada vary, with altitudes of 627.76 to 941.88 m above sea level.

2.9.7. Mean of building height factor

The average height of the buildings located within each LCZ affects the reflectivity, air flow and heat transfer on the ground surface of the study area, in turn influencing the urban climate (Khamchiangta and Dhakal, 2019). The heights of Granada's buildings were taken from data of the Geographic Information System (GIS) of the Electronic System of the Cadastre. The arithmetic mean was used to calculate the mean height of the building. Depending on the LCZ, average building heights in the city range from 1.25 to 5.24 stories.

2.9.8. Number of vehicles as a factor

The anthropogenic heat of the vehicles circulating through the city is another important element when studying factors that affect the UHI (Khamchiangta and Dhakal, 2019; Romero et al., 2020), especially considering that Granada has one of the highest levels of pollution in all of Spain. This value was obtained from the inventory of the mobile fleet of the Governmental Administration of the city.

Average motorization factors, depending on the LCZ, vary widely: between 200 and 418 vehicles per 1000 inhabitants.

2.9.9. Population density

Population density is closely related to human activities and anthropogenic heat in cities (Khamchiangta and Dhakal, 2019; Romero et al., 2020), being linked to heat emissions from travel demand and energy consumption. The population density in the city of Granada was divided, in view of the LCZ, into groups varying between 8 people / km² and 261 people / km². For its calculation, the population data of the city were taken from the Geographic Information System (GIS) of the Cadastre Electronic System.

2.9.10. Sky view factor

The Sky View Factor (SVF) is a pertinent parameter that has been widely used to measure the impact of urban geometry on city temperatures (Chun and Guldmann, 2014; Dirksen et al., 2019; Khamchiangta and Dhakal, 2019; Hu et al., 2020). The SVF affects warming potential due to reflected radiation; it is defined as the ratio between the visible area of the sky and the portion of the sky obstructed by diverse architectural and environmental elements (buildings, trees, etc.). Its value is dimensionless, and varies between 0 and 1. A value of 0 indicates that all outgoing radiation is completely blocked by objects, while a value of 1 indicates that all outgoing radiation will be freely distributed in the sky.

To calculate and map the SVF, SAGA simulation software for QGIS was used, the details and trigonometric formulas being available in Häntzschel et al. (2007) and Zakšek et al. (2005). To this end, and based on the Digital Terrain Model and the Digital Map of Surfaces obtained from the Geographic Information System (GIS) of the National Center for Geographic Information of Spain's Ministry of Transportation, a simulation was carried out in SAGA. Upon completion, the results were exported to QGIS to determine the mean SVF values for each LCZ.

2.10. Analysis strategy

Statistical analysis of the data collected in this study was performed with the help of specialized software, STATA version 15. Input was divided into two phases: the first involved analysis of the data from Sentinel day and night, but separately, in order to identify factors affecting the city's daytime and nighttime UHI. Secondly, the results of the analysis of Sentinel day and night data for each LCZ were explored in order to find the factors that would specifically affect the day and night UHI of each area. Both phases were carried out using the Data Panel technique, which is widely used in the literature for intervening statistical analysis, and features multivariate relational models (Chen et al., 2011; Alcock et al., 2015; Fang and Tian, 2020). This method allows for a greater number of data in the analysis, thereby increasing the degree of freedom, while reducing inconvenient collinearity between the variables (Smith and Hsiao, 1988). By taking into account individual effects, the final function obtained for the set of individuals is totally different from the one that would have been obtained using other statistical techniques (Labra, 2014). The method is recommended for dealing with time series involving multiple individual and quantitative variables, where explanatory variables in the relations between individuals might change (Seto and Kaufmann, 2003). Hence, this system of analysis was very well suited to the experimental data of our study.

Introducing this method of statistical analysis in our model entailed two phases (Chen et al., 2011). Firstly, by means of the Hausman proof, the effects of the analysis were determined to be either fixed or random. Then the model was assessed in view of the results obtained in Wooldridge and Wald Tests. There are three options for calculation: Method of Ordinary Squares (MOS), Generalized Least Squares (GLS) and the Method of Intragroup Estimators (MIE) (Labra, 2014).

The first of the three, while widely used for years, does not enable the effects of every individual to be analyzed over the course of time, which can give rise to biased estimators.

The second is considered to be a more efficient extension of the first. It is assumed that individual effects are not reflected in the explanatory variables of the model; instead, they contribute to the error term, following the expression:

$$Y_{it} = \beta X_{it} + (\alpha + \mu_{it}) \quad (4)$$

where α_i represents the individual effects, μ_{it} is the error of the model, X would represent explanatory variables, $i=\text{individual}$ and $t=\text{time}$.

The third method cited above assumes that individual effects are in line with the explanatory variables, so that the individual effect is separated after error, under the following calculation:

$$Y_{it} = \alpha_i + \beta X_{it} + \mu_{it}, \quad (5)$$

where, again, α_i are the individual effects, μ_{it} is the error of the model, X are explanatory variables, $i=\text{individual}$ and $t=\text{time}$.

3. Results

3.1. Land surface temperature sentinel day- and night-related local climate zone classification

The LST statistics obtained by means of Sentinel day and night products, and in situ using temperature probes, are shown in Fig. 7.

In general terms, Sentinel day and night present higher annual mean values than those obtained in situ using temperature probes. Specifically, in the morning, the highest mean LST values are obtained using the official product Sentinel day (299.62 K), while the mean in situ LST was lower (296.15 K). At night, the highest mean LST values were obtained using the official Sentinel night product

(285.47 K), while the mean LST in situ was lower (282.60 K). The mean differences obtained between the LSTs were 3.47 K for Sentinel day and 2.87 K for Sentinel night. Fig. 7 reflects the positive asymmetry of daytime LST data, with values concentrated in the third quartile. In contrast, the nocturnal LST data exhibit negative asymmetry, concentrating values in the first quartile. Both the day and night data show more variability among the lowest 25% of the values, the difference being greater for nighttime values.

The statistics of the LST for each LCZ obtained using Sentinel day and night products are shown in Fig. 8.

Fig. 8 (a) shows the mean daytime LSTs for the different climatic zones of the city of Granada. They are seen to present very similar values: Open High-Rise (300.11 K), Compact High-Rise (299.66 K), Compact Low-Rise (299.43 K) and Open Low-Rise (299.29 K). The standard deviations of each LCZ are respectively 11.95 K, 12.15 K, 12.53 K and 12.14 K. High-density areas are found to have an above-average LST, while low-density areas have a below-average LST. The average temperature difference between high- and low-density areas was 0.52 K, while the average difference between the highest and lowest temperatures was 0.82 K, corresponding to Open High-Rise and Open Low-Rise areas.

Fig. 8 (b) shows the average night LST for the different climatic zones of Granada. Although they present similar values, the slight differences should be noted: Compact High-Rise (286.32 K), Compact Low-Rise (285.69 K), Open High-Rise (285.43 K) and Open Low-Rise (284.44 K). The standard deviations of each LCZ were respectively 8.29 K, 8.80 K, 8.98 K and 9.09 K. The compact areas present an LST above the average, the open areas below the average. The average difference between compact and open areas was 1.06 K, yet the average difference between the areas with the highest and lowest temperatures was 1.88 K, corresponding to the Compact High-Rise versus Open Low-Rise areas. The LST data from both Sentinel day and night for the LCZ present greater variability of the data among the 25% lowest values, this difference proving greater in the nocturnal LSTs. Likewise, the difference in temperatures registered—between the hottest and coldest local area—is twice as high at night as in the morning.

The Mean Bias Error (MBE) values obtained for Sentinel day and night were -0.1355 and 0.0237 , respectively. The Root Mean Square Error (RMSE) values obtained for Sentinel day and night were respectively 2.815 K and 3.116 K. For Sentinel day, the MBE values obtained for each of the LCZs were -0.139 K, -0.1153 K, -0.207 K and -0.118 K, respectively. The RMSE values obtained for each of the LCZs were respectively 3.089 K, 2.739 K, 2.858 K and 2.619 K. For Sentinel night, the MBE values obtained for each LCZ were 0.167 K, 0.021 K, 0.1376 K and -0.078 K, respectively. The RMSE values obtained for each LCZ were 3.206 K, 3.289 K, 3.036 K and 2.848 K, respectively.

Analysis of the ambient temperatures obtained in situ with the eighteen probes distributed throughout the city brings up some important questions. Over the period studied, there are measurement differences among the different LCZs and among the different probes located within each LCZ typology. In both cases, these differences are smaller in the morning than at night. Accordingly, the average ambient temperature taken by the probes for each LCZ in the Sentinel day passage schedule was: Compact High-Rise (296.30 K), Compact Low-Rise (296.10 K), Open High-Rise (296.15 K), Open Low-Rise (296.05 K), Scattered Trees (296.43 K) and Low Plants (297.44 K). The greatest difference in mean values between LCZs was 1.39 K. The temperature differences between probes of each LCZ during daytime were: Compact High-Rise (2.00 K), Compact Low-Rise (0.65 K), Open High-Rise (0.31 K) and Open Low-Rise (0.03 K). The mean ambient temperature taken by the probes for each LCZ in the Sentinel night passage schedule was: Compact High-Rise (282.90 K), Compact Low-Rise (282.31 K), Open High-Rise (282.80 K), Open Low-Rise (282.40 K), Scattered Trees (281.70 K) and Low Plants (281.10 K). The greatest difference in the mean values between LCZs was 1.80 K. The temperature differences between probes of each LCZ at nighttime were: Compact High-Rise (3.45 K), Compact Low-Rise (0.80 K), Open High-Rise (0.41 K) and Open Low-Rise (0.06 K). As can be seen, the greatest differences in measurement, either in the morning or at night, are obtained in the compact areas as opposed to the open areas. In turn, the probes of the same LCZ typology were found to record higher temperatures in urban areas in the center of the city. The lowest temperatures obtained by probes within the same LCZ typology correspond to suburban areas, on the outskirts of the city.

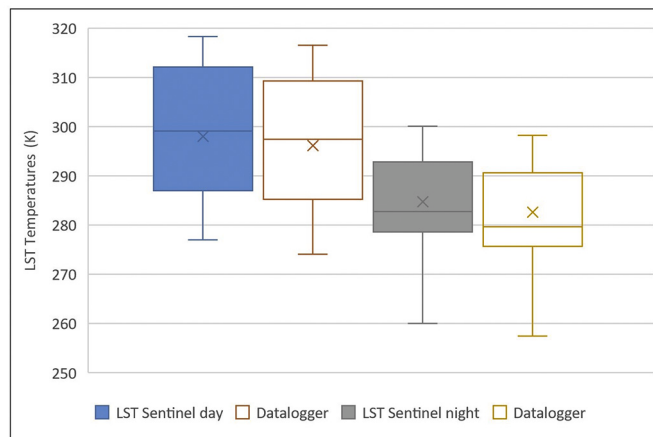


Fig. 7. LST Sentinel day and night LST in situ.

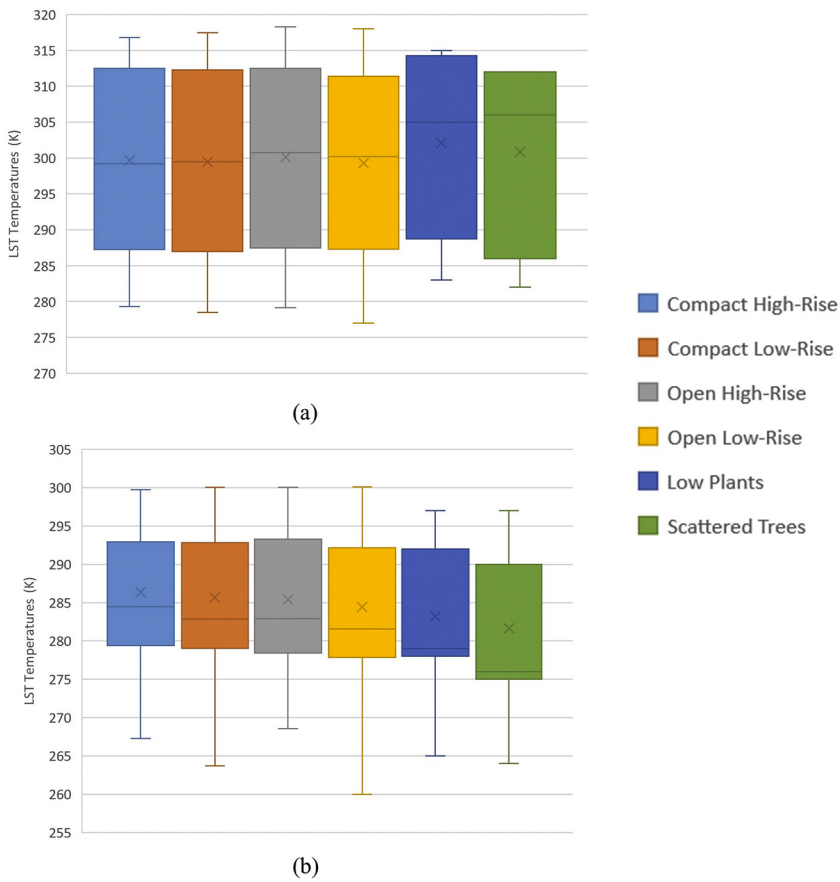


Fig. 8. LST Sentinel day and night by Local Climate Zone.

3.2. Local climatic zones classified with regard to the intensity of the UHI

The UHI statistics obtained by means of Sentinel day for each LCZ are shown in Fig. 9.

Fig. 9a shows the mean UHI intensity recorded during the study period for each LCZ in the city of Granada on the basis of Sentinel day images. The average diurnal intensity of UHI in the city was -0.60 K . The highest UHI intensities correspond to shades of red, and they are found in the outer rural areas devoid of vegetation cover. Shades of blue, green and yellow indicate negative UHI values and are located within urban areas. This circumstance indicates that, during the morning, temperatures in rural areas are higher than temperatures in urban areas. In the early morning hours, solar radiation is higher in these areas than in the inner city, owing to the shade beside buildings and trees, the heterogeneous system of impermeable walls, and high thermal absorption and cooling rates undergone by vegetated areas, as opposed to the warming rates of areas with sparse vegetation and bare soils. Thus, the shade generated by city buildings and trees blocks solar radiation from heating the waterproof walls of urban areas, which would lead to high doses of heat altering the LST of the area (Li and Meng, 2018; Lemus et al., 2020; Yang et al., 2020a). Numerous studies involving satellite images show that vegetation has a cooling effect on urban areas (Lin et al., 2015; Du et al., 2017; Yu et al., 2017) that oscillates between 1 and 3 K (Lin et al., 2015), as well as a warming effect in areas with scarce vegetation and/or bare soils (Xiao and Weng, 2007; Estoque et al., 2017). Such effects are not only due to shading and evapotranspiration processes, but also depend on the rates of cooling or heating by convection and transpiration, which would alter a zone's LST and explain the daytime and nighttime behaviors of the UHI.

Fig. 9b offers the diurnal mean UHI values for each LCZ: Compact High-Rise (-0.01 K), Open High-Rise (-0.18 K), Compact Low-Rise (-0.42 K) and Open Low-Rise (-1.05 K). The standard deviation values for each LCZ are respectively 2.43 K , 3.23 K , 3.42 K and 3.84 K . The maximum intensities reached in each LCZ throughout the study period were: Compact High-Rise (4.06 K), Open High-Rise (4.02 K), Open Low-Rise (3.95 K) and Compact Low-Rise (3.93 K). The high-density areas are seen to have a lower negative UHI value and a higher maximum intensity; the low-density areas, in turn, have a higher negative UHI value and a lower maximum intensity. The average difference in UHI between high-rise and low-rise zones was 0.64 K . The average difference obtained between the zones with the highest and lowest temperatures —the Compact High-Rise and Open Low-Rise zones— was 1.04 K .

The statistics of the UHI obtained using the Sentinel night products for each LCZ are shown in Fig. 10. Fig. 10a shows the mean UHI intensity recorded during the study period for each LCZ in the city of Granada based on Sentinel night images. The average nighttime

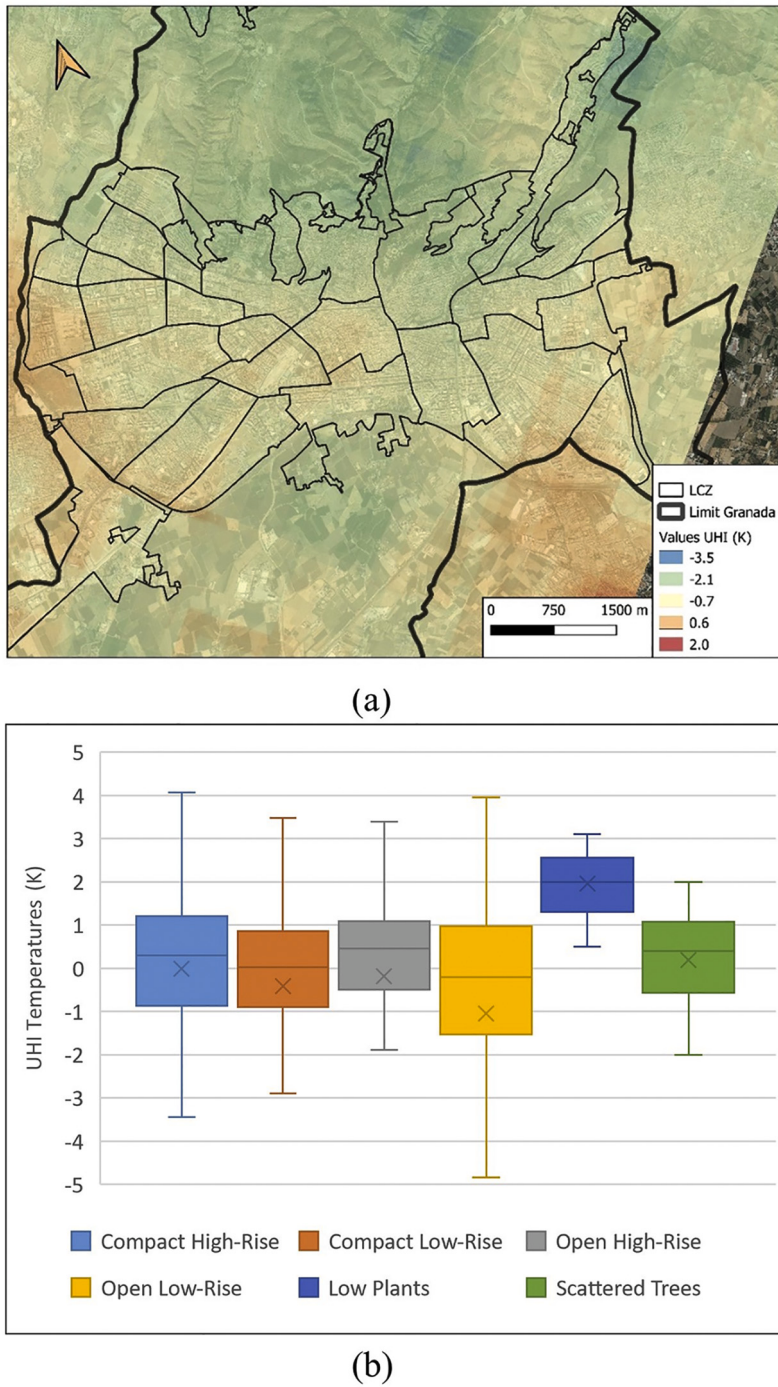


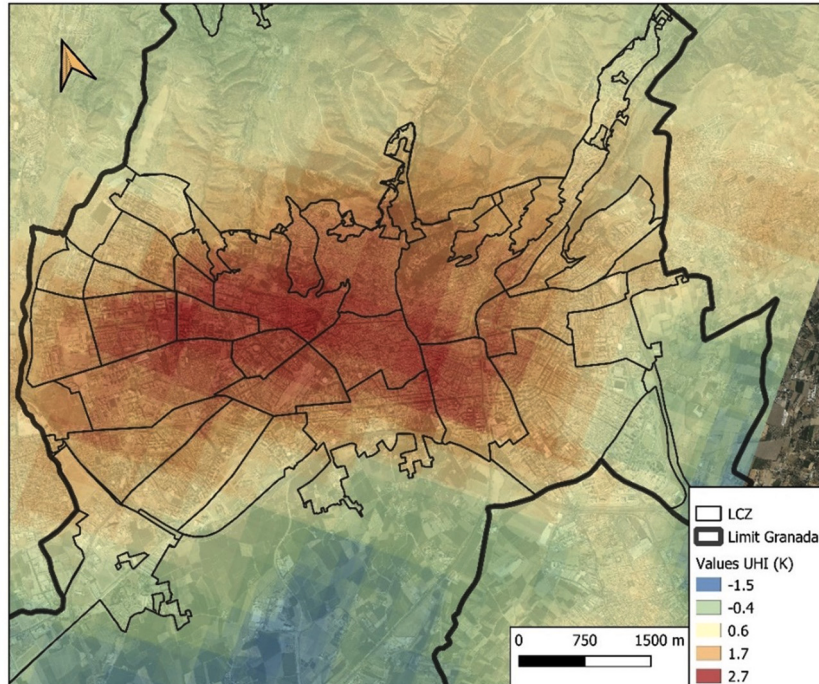
Fig. 9. UHI Sentinel day by Local Climate Zone. Image source: The National Geographic Institute (Spain's Ministry of Transport).

UHI intensity of the city was +0.70 K. The highest UHI intensities, viewed in shades of red, are located in the inner urban areas. Blue and green indicate negative UHI values, found in areas bordering the city. In other words, at night the temperatures of rural areas are lower than those of urban areas, because once the sun sets, rural areas tend to cool down rapidly, but urban areas retain heat.

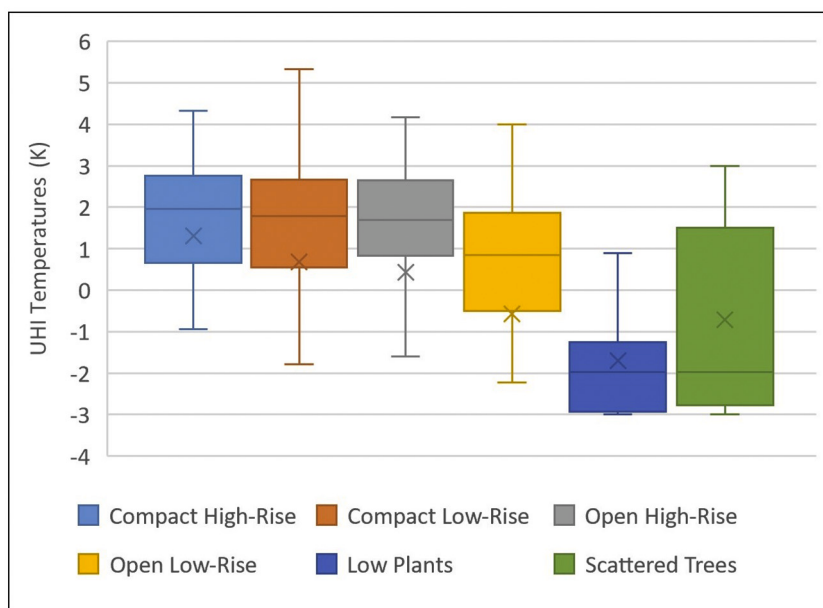
Fig. 10b shows the mean night UHI values for each LCZ: Compact High-Rise (1.32 K), Compact Low-Rise (0.68 K), Open High-Rise (0.42) and Open Low-Rise (-0.57 K). The standard deviation values of each LCZ are 3.38 K, 5.02 K, 5.25 K and 5.90 K, respectively. The mean difference in UHI between compact and open areas was 0.93 K. The average difference obtained between the areas with the highest and lowest temperatures was 1.89 K, corresponding to the Compact High-Rise versus Open Low-Rise areas. The maximum

intensities reached in each LCZ throughout the study period were: Open High-Rise (6.46 K), Compact Low-Rise (5.33 K), Compact High-Rise (4.31 K) and Open Low-Rise (4.00 K).

Although the values of the physical properties of the LCZs of our study are within the ranges of standard LCZ values provided by authors [Stewart and Oke \(2009\)](#), significant differences are observed with respect to the daytime UHI values obtained with Sentinel. The differences were positive in urban areas and negative in rural areas. The results are as follows: Compact High-Rise (+3.90 K), Compact Low-Rise (+1.28 K), Open High-Rise (+1.82 K), Open Low-Rise (-0.05 K), Scattered Trees (-0.80 K), and Low Plants (-5.05



(a)



(b)

Fig. 10. UHI Sentinel night by Local Climate Zone. Image source: The National Geographic Institute (Spain's Ministry of Transport).

K). The nocturnal UHI values obtained with Sentinel are generally within the temperature ranges reported by the cited authors, and the nighttime differences for urban and rural areas were negative. The differences found by each LCZ were: Compact High-Rise (-1.28 K), Compact Low-Rise (-0.32 K), Open High-Rise (-1.08 K) and Open Low-Rise ($+0.17$ K), Scattered Trees (-0.20 K), and Low Plants (-0.90 K).

3.3. UHI seasonality

Many authors warn of the variability existing in the intensity of UHI in a city during the different seasons of the year (Zhou et al., 2014; Fu and Weng, 2018; Peng et al., 2018; Hu et al., 2020). The results reported here also reflect such variability among stations, for the data from both Sentinel day and night. Fig. 11 shows the UHI results obtained in Granada using Sentinel day during the four seasons.

It is evident that throughout the year there is considerable variability regarding the intensity and the affected areas of the city. The mean UHI is negative during the autumn, spring and summer, while intensity is positive in the winter season. Along general lines and throughout the year, the city is represented by green and blue tones, with red tones being located in suburban or rural areas. This denotes that the outer areas of the city have higher temperatures than the inner areas. The mean UHI values for the city of Granada by season were: autumn (-1.51 K), winter (1.67 K), spring (-4.02 K) and summer (-2.62 K). The maximum intensity was obtained in the

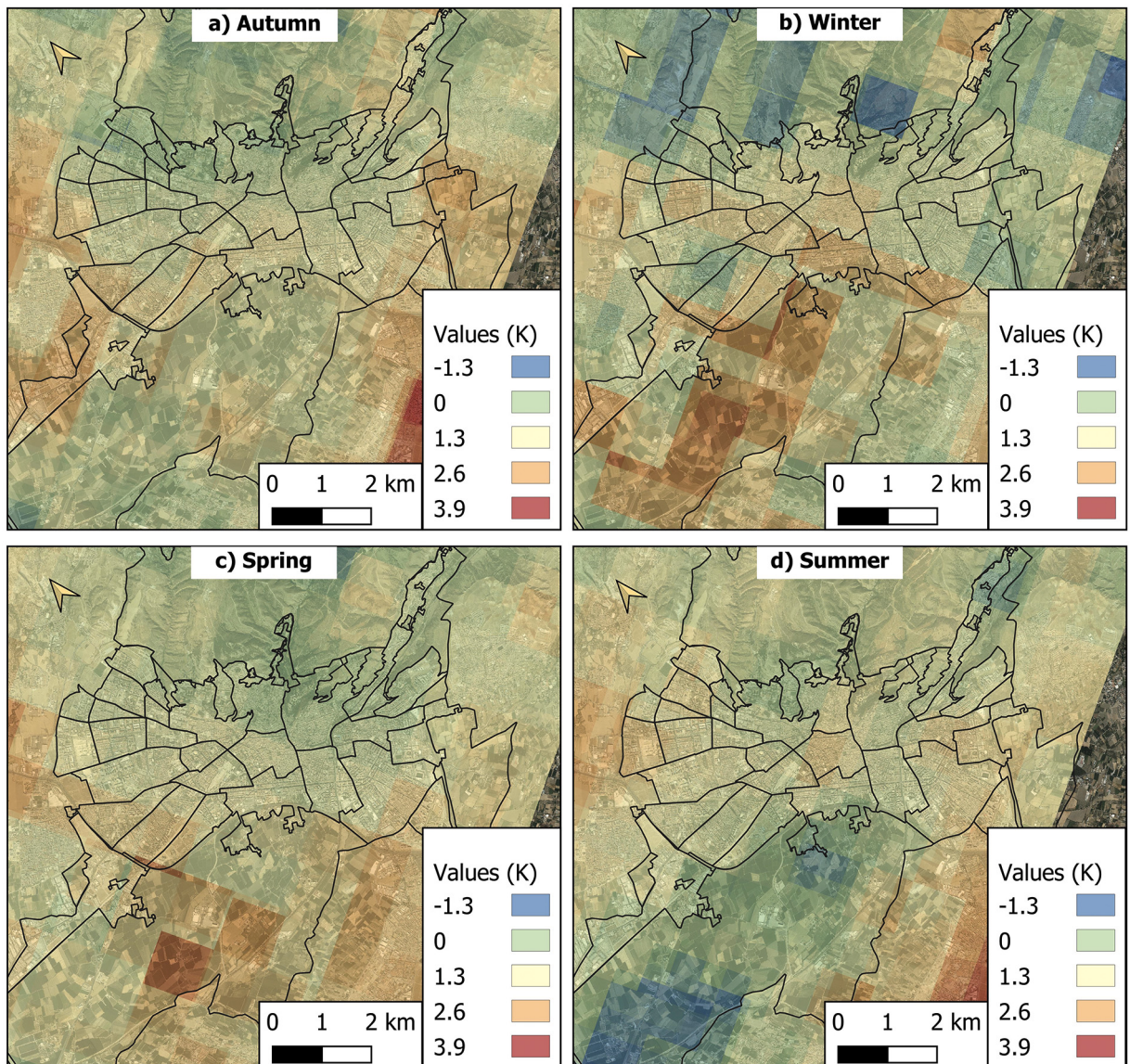


Fig. 11. UHI seasonality obtained with Sentinel day. Image source: The National Geographic Institute (Spain's Ministry of Transport).

spring.

Fig. 12 presents the UHI results for Granada obtained by Sentinel night during the four seasons, making evident the variability throughout the year of the intensity and the affected areas of the city at the moment when Sentinel night passed. In this case positive UHI values were obtained during all four seasons. Overall and throughout the year, the city is represented by red tones, with green and blue tones for the outer areas of the city having lower temperatures. The mean UHI values for the city of Granada obtained for each season were: autumn (2.10 K), winter (0.53 K), spring (0.69 K) and summer (0.85 K). The maximum intensity was obtained in autumn, the other three seasons presenting very similar values.

Fig. 13 shows the UHI statistics with Sentinel day and night for each LCZ and for each station. Note the variability that the UHI presents in each LCZ per station. Accordingly, the UHI obtained through Sentinel day images in spring shows the highest intensities in the LCZs Scattered Trees, Open Low-Rise and Compact Low-Rise; the lowest intensities are found for LCZs Open High-Rise and Low Plants. In contrast, the UHI obtained by Sentinel night images during the fall shows the highest intensities in the LCZs Compact High-Rise, Compact Low-Rise and Scattered Trees, whereas the lowest intensities are seen for the LCZs Low Plants, Open Low-Rise and Open High-Rise.

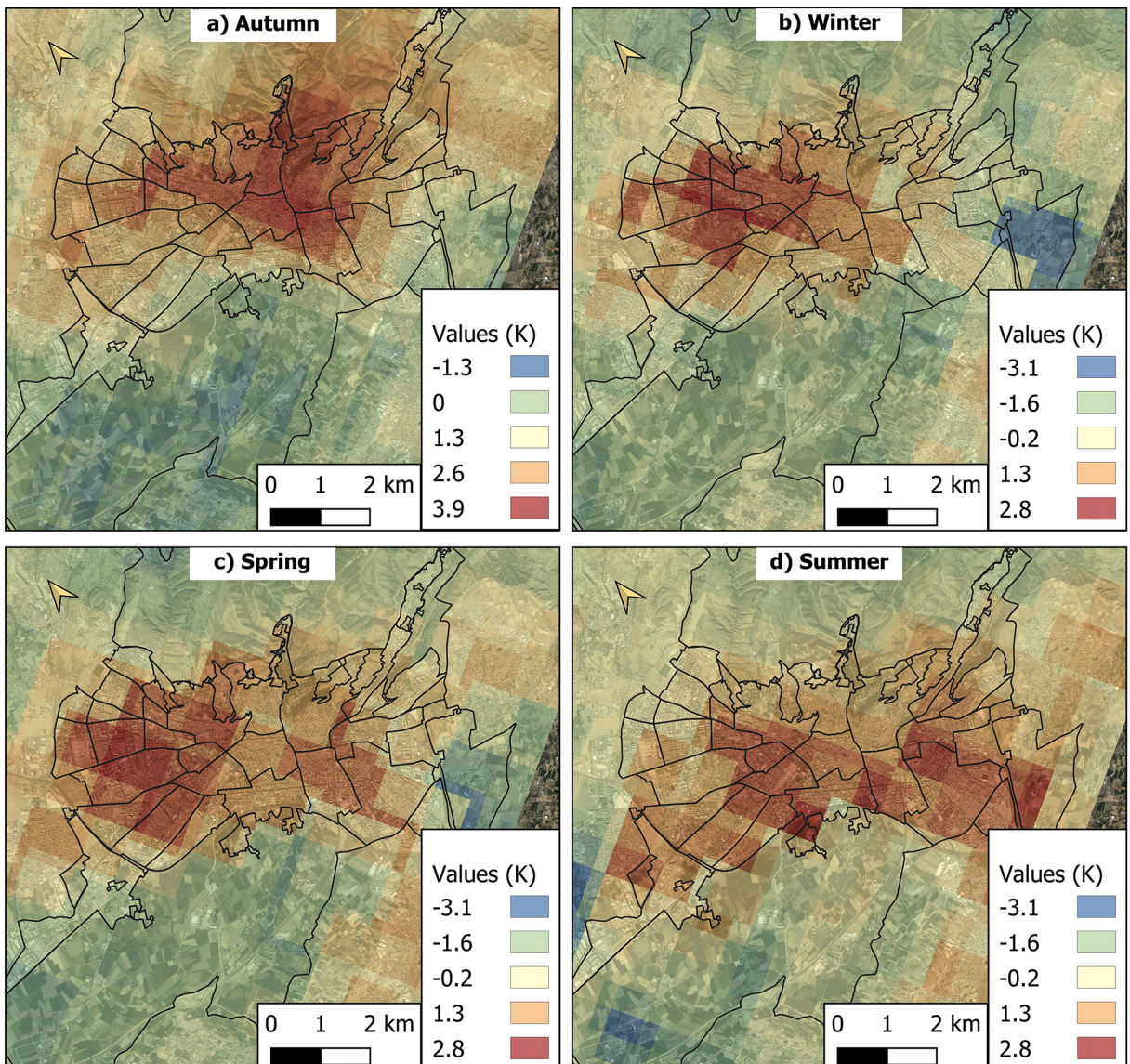


Fig. 12. UHI seasonality obtained with Sentinel night. Image source: The National Geographic Institute (Spain's Ministry of Transport).

3.4. Statistical analysis

First, we determined the R^2 coefficients of linear adjustment between the LST with Sentinel day and night and the LST obtained in situ. The results are considered adequate since they present values above 0.94 (Sentinel day $R^2 = 0.95$ and Sentinel night $R^2 = 0.97$), and are considered statistically significant. The standard deviation (SD) obtained for the Sentinel day data set was 12.12 K, while for the Sentinel night data it was 8.78 K.

Next, using Data Panel, statistical analysis of the factors that could influence the daytime and nighttime UHI was performed. As a first step, it was necessary to determine whether the calculation procedure should be carried out using fixed or random effects. To this end the Hausman test was implemented, it indicating that the panel of robust random effects was needed for the data obtained both in the first phase and in the second phase of the analysis. To develop the Data Panel, the of Generalized Least Squares (GLS) method was used, applying Eq. 4.

The results of analysis of the diurnal and nocturnal UHI data from Sentinels day and night are indicated in Table 7.

The results of the statistical analysis of the UHI data obtained by means of Sentinel day images indicate that there is a statistically significant relationship above 99% with the independent variables solar radiation and altitude. The relationship becomes statistically significant at 99% for the variables Pv and population density, and statistically significant at 95% for the variables ISA, fraction of building height factor and number of vehicles as a factor.

The statistical analysis of the UHI data from Sentinel night images indicate a statistically significant relationship above 99% with the independent variables Pv, solar radiation and altitude. This relationship becomes statistically significant at 99% for the variables wind, ISA, and SVF, and statistically significant at 95% for the variable number of vehicles as a factor.

In the statistical analysis of the diurnal data from Sentinel day, eight variables were statistically significant at 95%, while with the nocturnal data from Sentinel night, seven variables were obtained. Altitude, number of vehicles and solar radiation maintain the percentage of significance both in the morning and at night. Pv increases significance in the nighttime UHI data. Pollution, fraction of facades and population density were statistically significant when calculating the diurnal UHI but not for the night UHI; the variables wind and SVF were statistically significant for the determination of the night UHI.

The values obtained for R^2 and the F statistic of the UHI data for Sentinels day and night are shown in Table 8. Good concordance is seen between the dependent variable and the independent variables, with a level of adjustment up to 99% of significance, since Prob>chi2 = 0.000.

The results of the analysis of the UHI data obtained using Sentinels day and night for each LCZ are indicated in Tables 9 and 10.

Statistical analysis of the UHI data from Sentinel day images for the Compact High-Rise areas point to a statistically significant relationship above 99% for the independent variable solar radiation, and of 99% for the variable NDBI. When taking the UHI data from Sentinel night for the same compact areas, a statistically significant relationship occurs above 99% for the independent variable Pv and at 95% for the variables wind, building fraction factor, altitude, motorization factor of vehicles, population density and SVF. Therefore, in these areas, the two variables that affect daytime UHI with the greatest intensity are NDBI and solar radiation, whereas Pv is the most significant factor for nighttime UHI.

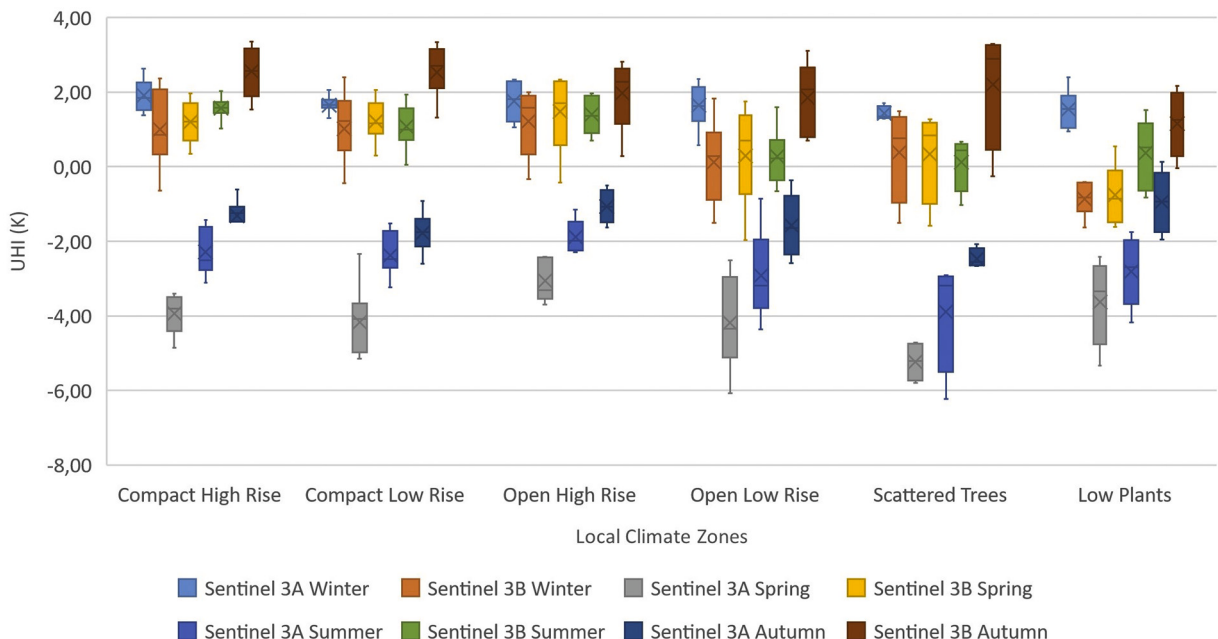


Fig. 13. UHI statistics with Sentinel day and night for each LCZ and for each station.

Table 7

ata panel results for Sentinels day and night: relationships between variables.

Satellite	Sentinel day			Sentinel night		
	β	p	sd	β	p	sd
NDVI	-2.086	0.212	1.673	2.230	0.473	3.094
PV	-10.223	0.005**	3.654	-28.587	0.000***	3.756
NDBI	-8.026	0.400	9.536	18.470	0.077	10.461
Contamination	0.026	0.029*	0.012	0.004	0.614	0.009
Solar radiation	0.003	0.000***	0.001	0.001	0.000***	0.000
Wind	0.002	0.077	0.001	-0.006	0.001**	0.002
Impervious Surface Fraction Factor	0.010	0.039*	0.005	0.026	0.001**	0.008
Fraction of building facades	0.336	0.031*	0.016	0.030	0.198	0.023
Altitude	-0.013	0.000***	0.002	-0.021	0.000***	0.004
Mean of Building Height Factor	-0.042	0.692	0.107	-0.084	0.661	0.192
Number of Vehicles as a Factor	-0.002	0.016*	0.001	-0.004	0.042*	0.002
Population Density	0.004	0.006**	0.002	-0.007	0.069	0.004
Sky View Factor	-3.785	0.063	2.034	-12.579	0.001**	3.702
Constant	1170,581	0.000***	2.438	23.055	0.000***	5.180

β: Coefficient; sd: Standard deviation; Robust Standard Errors: * $p < 0.05$, ** $p < 0.01$ and *** $p < 0.001$.

Table 8 R^2 and F UHI statistical analysis.

Satellite	R^2	F	Prob>chi2
Sentinel day	0.717	2640	0.000
Sentinel night	0.636	357.7	0.000

R^2 : Linear fitting coefficient. F: F statistic.

Statistical analysis of the UHI data obtained with Sentinel day images for the Compact Low-Rise areas gives a significant relationship above 99% for the independent variable solar radiation. The relationship is statistically significant at 99% for the variable building surface fraction factor, and at 95% for the variables NDBI, altitude, mean building height factor and SVF. For the same areas, but with the UHI data taken from Sentinel night images, there is a statistically significantly relationship of 99% for the independent variables Pv, solar radiation and SVF. The relationship becomes statistically significant at 99% for the variables ISA and building surface fraction factor. Meanwhile, the independent variables NDVI, altitude and mean of building height factor are statistically significant at 95%. Therefore, in these areas the two variables that most affect the daytime UHI are solar radiation and the building surface fraction factor, Pv; solar radiation and SVF are the most significant factors for night UHI.

The analysis of UHI data from Sentinel day images for the Open High-Rise areas gives a statistically significant relationship above 99% for the independent variables solar radiation, NDBI, and building surface fraction factor. The relationship is at 99% for the variables NDVI and wind, and 95% for the variable SVF. For the same areas, but with the UHI data from Sentinel night, a statistically significant relationship above 99% is seen for the independent variables NDBI and SVF. Significance is 99% for the variables solar radiation, building Surface fraction factor and mean of building height factor, and 95% for the variable population density. Thus, in these areas, the three variables most affected by daytime UHI are NDBI, solar radiation and building surface fraction factor. NDBI and SVF are the most significant factors in night UHI.

The analysis of UHI data from Sentinel day images of the low-density open areas indicate that there is a statistically significant relationship of 99% for pollution and wind, and of 95% for the variables Pv and solar radiation. For the same areas, but with the UHI from Sentinel night, a statistically significant relationship is produced above 99% for the independent variables Pv and NDBI, and at 99% for the variables NDVI, wind and altitude. In these areas the two variables that most affect daytime UHI are therefore pollution and wind, whereas Pv and NDBI are the most significant factors in nighttime UHI.

The values obtained for R^2 and the F statistic of the UHI data for Sentinels day and night by LCZ are shown in Table 11. There is good agreement between the dependent variable and the independent variables, with a level of adjustment up to 99% of significance (Prob> chi2 = 0.000).

4. Discussion

The results of the level 2 products of Sentinel day and night in obtaining LST and UHI for the city of Granada would indicate adequate, consistent yields, in line with those reported by similar studies (Li et al., 2011; Tan and Li, 2015; Sobrino et al., 2016; Prikaziuk and van der Tol, 2019; Chiang, 2020; Hu et al., 2020; Yang et al., 2020a; Yang et al., 2020b).

In general terms, the mean LSTs obtained with Sentinel 3 products are higher than the LSTs determined in situ. According to the Sentinel day data, the mean daytime LST is 3.47 K above the in situ LST, and the difference is of 2.87 K in the case of Sentinel night. The R2 coefficients of determination are above 0.94, denoting a good agreement of the values and an adequate general performance. Similar findings have been reported by previous authors in other cities or territories (Coppo et al., 2010; Ruescas et al., 2016; Sobrino

Table 9

Data panel results for Sentinels day and night by LCZ: relationships between variables.

Satellite	LCZ			Compact high-rise						Compact low-rise					
	Sentinel day			Sentinel night			Sentinel day			Sentinel night					
	β	p	sd	β	p	sd	β	p	sd	β	p	sd	β	p	sd
NDVI	-2.005	0.772	6.929	-5.364	0.416	6.590	3.403	0.064	1.834	9.206	0.016*	3.817			
PV	1.348	0.875	8.590	-27.03	0.000***	7.259	2.939	0.499	4.348	-32.466	0.000***	5.474			
NDBI	46.415	0.001**	14.095	-23.43	0.108	14.584	-28.53	0.014*	11.603	5.062	0.780	18.143			
Contamination	-0.040	0.097	0.241	-0.009	0.717	0.024	0.000	0.991	0.172	0.005	0.789	0.017			
Solar radiation	0.006	0.000***	0.002	0.001	0.197	0.001	0.005	0.000***	0.001	-0.002	0.000***	0.001			
Wind	0.041	0.482	0.058	-0.120	0.025*	0.054	0.002	0.164	0.002	0.008	0.099	0.005			
Impervious Surface Fraction Factor	-0.220	0.191	0.168	0.361	0.047*	0.185	0.400	0.142	0.027	0.142	0.003**	0.048			
Building Surface Fraction Factor	0.305	0.124	0.198	0.444	0.042*	0.218	0.134	0.001**	0.384	0.204	0.001**	0.611			
Altitude	2.196	0.235	1.848	3.967	0.049*	2.019	-0.010	0.041*	0.005	-0.020	0.010*	0.008			
Mean of Building Height Factor	4.901	0.281	4.548	8.615	0.090	5.085	1.019	0.015*	0.421	1.807	0.012*	0.723			
Motorization factor of vehicles	0.460	0.232	0.385	0.833	0.046*	0.417	0.001	0.214	0.001	0.003	0.103	0.002			
Population Density	0.595	0.230	0.496	1.085	0.048*	0.542	0.000	0.867	0.001	0.004	0.104	0.002			
Sky View Factor	568.016	0.227	470.429	-1011.44	0.049*	515.021	25.735	0.010*	-9.980	48.439	0.000***	10.451			
Constant	-2203.6	0.234	1852.5	-3978.4	0.049*	3024.2	-23.359	0.020*	10.031	-53.038	0.000***	11.859			

β: Coefficient; sd: Standard deviation; Robust Standard Errors: *p < 0.05, **p < 0.01 and ***p < 0.001.

Table 10

Data panel results for Sentinels day and night by LCZ: relationships between variables.

LCZ		Open high-rise						Open low-rise					
Satellite		Sentinel day			Sentinel night			Sentinel day			Sentinel night		
		β	p	sd	β	p	sd	β	p	sd	β	p	sd
NDVI		6.923	0.005**	2.476	18.872	0.097	11.385	-4.380	0.388	5.080	11.401	0.003**	3.793
PV		-11.629	0.149	8.060	-17.110	0.220	13.938	61.748	0.035*	29.258	-52.118	0.000***	12.68
NDBI		44.206	0.000***	8.071	130.20	0.000***	24.623	73.366	0.140	49.656	81.429	0.000***	18.93
Contamination		0.035	0.280	0.032	-0.019	0.417	0.024	0.069	0.001**	0.021	-0.006	0.842	0.029
Solar radiation		0.006	0.000***	0.001	-0.002	0.002**	0.001	0.003	0.049*	0.004	-0.001	0.125	0.001
Wind		-0.188	0.001**	0.058	-0.173	0.018	0.073	-0.088	0.009**	0.034	-0.207	0.002**	0.067
Impervious Surface Fraction Factor		0.037	0.089	0.022	-0.060	0.245	0.052	-0.154	0.598	0.029	0.014	0.638	0.029
Building Surface Fraction Factor		-0.150	0.000***	0.020	-0.379	0.001**	0.117	0.065	0.466	0.089	0.091	0.349	0.097
Altitude		0.000	0.939	0.006	0.116	0.432	0.015	-0.008	0.497	0.012	-0.028	0.006**	0.101
Mean of Building Height Factor		0.459	0.086	0.268	2.487	0.007**	0.926	0.100	0.806	0.409	-0.110	0.844	0.560
Motorization factor of vehicles		-0.001	0.944	0.013	0.013	0.090	0.001	-0.001	0.915	0.009	-0.010	0.230	0.009
Population Density		-0.011	0.286	0.010	0.012	0.023*	0.002	0.031	0.315	0.031	0.005	0.814	0.022
Sky View Factor		18.486	0.010*	8.765	58.57	0.000***	9.834	13.930	0.324	14.131	-3.913	0.731	11.37
Constant		-0.872	0.862	5.027	-3.541	0.706	9.390	-18.958	0.452	25.225	15.875	0.417	19.54

β: Coefficient; sd: Standard deviation; Robust Standard Errors: *p < 0.05, **p < 0.01 and ***p < 0.001.

Table 11 R^2 and F UHI by LCZ statistical analysis.

LCZ	Satellite	R^2	F	Prob>chi2
Compact High-Rise	Sentinel day	0.899	2140	0.000
	Sentinel night	0.806	450	0.000
Compact Low-Rise	Sentinel day	0.731	430	0.000
	Sentinel night	0.812	145	0.000
Open High-Rise	Sentinel day	0.710	23.5	0.000
	Sentinel night	0.750	1717	0.000
Open Low-Rise	Sentinel day	0.690	21.6	0.000
	Sentinel night	0.650	12.1	0.000

R^2 : Linear fitting coefficient. F: F statistic.

et al., 2016; Prikaziuk and Van der Tol, 2019; Chiang, 2020; Yang et al., 2020a), which lends validity to the results obtained here. The LST results obtained in the present investigation, together with the high concordance with similar investigations, suggest that the climatic conditions and high pollution to which the city of Granada is exposed do not alter the precision of the LST obtained by the thermal bands of Sentinel satellites.

The LST data obtained using Sentinel day in the city of Granada reveal that high density LCZs show higher temperatures in the morning than low density LCZs. The mean difference in LST detected between the hot and cold daytime areas of the city was 0.82 K. In turn, the nighttime LST data obtained using Sentinel indicate that the LCZ of the highest temperature would be the compact areas. The mean difference in LST detected between the hot and cold night areas of the city was 1.88 K. The city's heterogeneous composition makes it possible to distinguish between compact areas with high LSTs that present high densities and large impervious areas, as opposed to suburban areas with relatively low temperatures that present lower densities and fewer impervious surfaces. Numerous studies corroborate such findings, showing that an increase in urbanized and impervious areas causes an increase in the LST of urban areas (Zakšek et al., 2005; Keramitsoglou et al., 2011; Feizizadeh and Blaschke, 2013; Mallick et al., 2013; Tsou et al., 2017; Barbieri et al., 2018; Li and Meng, 2018; Karakuş, 2019; Lemus et al., 2020; Yang et al., 2020a, 2020b).

The mean UHI value obtained with Sentinel day images, -0.60 K, reveals that the city has lower temperatures than the surrounding rural areas—a phenomenon referred to as an urban cooling island (Saaroni et al., 2018; Wu et al., 2019; Yang et al., 2020a). On the other hand, as the mean UHI data obtained by Sentinel night for the city was 0.7 K, Granada gives higher temperatures than the rural areas. According to the statistical analysis performed (using the Data Panel technique), both in the morning and at night, the independent variable solar radiation is statistically significant in a positive sense at 99%, so it can be considered as the most significant variable for the day and night UHI of the city of Granada. That is, the greater the solar radiation, the greater the intensity of the UHI, whose influence is decisive. This conditioning factor has been evoked in previous research (Ramamurthy and Bou-Zeid, 2017; Zhao et al., 2018) involving results from cities at latitudes between 38° and 43° north, as is the case of Granada. The fact that such cities tend to have some 2000–3000 h of sunshine per year underlines the relevance of the UHI. The independent variables—altitude and Pv—are negatively significant at 99%, pointing to a lower UHI intensity at higher altitude and/or PV. In the case of Granada, these variables are important because of the large variations between the different LCZs, both in altitude and in percentage of PV. These variables and their relationship with UHI have been addressed in previous research, with results similar to those obtained here (Gaur et al., 2018; Hua et al., 2020; Shafizadeh et al., 2020).

Apart from the previously mentioned variables, the results show us others that are not common, but are specific to day or night UHI. Thus, during the morning, factors such as environmental pollution and population density positively influence the UHI. Contrariwise, during the night, the factors are: Sky view factor, wind and ISA. Numerous investigations relate an increase in the intensity of the UHI to higher population density (Son et al., 2017; Song et al., 2020), % of facades (Dai et al., 2018; Hu et al., 2020), and contamination (Shafizadeh et al., 2020; Yao et al., 2018). To the contrary, a decrease in UHI may be tied to an increase in the sky view factor (Khamchiangta and Dhakal, 2019; Saaroni et al., 2018; Shafizadeh et al., 2020) or a higher wind speed (Van Hove et al., 2015).

The mean diurnal UHI according to LCZ appears to indicate that low-density areas have a greater negative UHI intensity; in high-density areas this value is reduced. In view of the data on maximum intensity of UHI detected, they would correspond to the high-density areas, in contrast to the lower UHI of lower-density areas. Again, solar radiation intervenes in a common way in different LCZs, as a statistically significant variable above 99% and in a positive sense. In a high-density LCZ, the NDVI factor minimizes the intensity of UHI. In contrast, in low-density LCZs it is the wind factor that minimizes the UHI. Authors Kim and Kim (2009) indicated that an increase in the height of buildings prevents adequate air circulation, which leads to higher concentrations of urban heat and an increase in LST and UHI. Chun and Guldmann (2014) reported that densely built-up areas of the city of Columbia generally exhibited higher temperatures than areas of low-density spaces, due to reduced air circulation and wind flow, and their related cooling effects. Such results, in conjunction with the research carried out by further authors (Garcia et al., 2018; Van Hove et al., 2015; Hu et al., 2020; Li et al., 2011; Saaroni et al., 2018; Sekertekin and Bonafoni, 2020; Song et al., 2020; Yang et al., 2020a, 2020b) come to support the values obtained in our research.

Regarding the nocturnal UHI according to LCZ, we might stress that compact areas show a greater positive UHI intensity, this value being reduced in open areas. The PV factor is seen to intervene in a common way in the different LCZs: as a statistically significant variable at 99% and in a negative way. In compact areas of the city, the sky view factor is statistically significant in a negative way. Yet in open areas the wind intervenes as a statistically significant variable in a negative way. Numerous studies using satellite images have shown that an increase in the vegetal fraction of urban areas has a cooling effect in the city (Du et al., 2017; Lin et al., 2015; Yu et al.,

2017) that could range between 1 and 3 K (Lin et al., 2015). A greater sky view in compact areas permits more dissipation of heat into the atmosphere, hence a lower UHI intensity (Alavipanah et al., 2018; Li and Zhou, 2019; Hu et al., 2020). Paradoxically—and although it may seem incompatible to increase both the plant fraction and the sky view in cities—a few recent studies (Chun and Guldmann, 2014; Hu et al., 2020) underline the positive effects of sky view on the decrease in UHI, citing values lower than 0.8.

With regard to the variability in the intensity and the areas affected by UHI, our results show that—according to Sentinel day—intensity is greater during the spring, and the lowest intensity occurs in the fall. In turn, the results from Sentinel night give the highest UHI intensity during the fall, and the lowest in winter. These values agree with other reports of seasonal variability in the UHI (Haashemi et al., 2016; Fu and Weng, 2018; Rui et al., 2018; Yang et al., 2020a), lending validity to the findings reported here. Such results may prove very meaningful for future studies focused on energy consumption and thermal comfort in homes in cities like Granada, and serve as a reference for endeavors intended to save energy and reduce environmental pollution.

The factors affecting the global UHI of the city and the UHI of each LCZ found should be considered relevant as sources of information for urban planners and the town council of the city of Granada, in particular, when weighing measures to mitigate the effects of the UHI, both at present and for the future, in light of the incorporation of new growth zones. Therefore, along general lines and after eliminating the environmental and geographical factors that we cannot modify, we may conclude that measures such as increasing the PV and reducing the ISA, reducing environmental pollution and population density, or increasing the view from the sky in each neighborhood, could help minimize the intensity of the UHI in the city of Granada. Future development might depend on the LCZ model chosen for new urban and peri-urban growth, meaning specific measures to mitigate the UHI could be adopted. Thus, in the case of compact and low-density areas, an increase in vegetation could be proposed up to a value of 0.8 in the sky view factor. In compact and high-density areas—as already indicated for low-density areas—it would be beneficial to seek an urban morphology that is receptive to the prevailing wind direction, as it is a significant element in Granada and its surroundings. Increasing the sky view and the NDBI factor would be advantageous for high-density open areas, while increasing the PV and NDBI and taking into account the prevailing wind direction would be advantageous for low-density open areas.

5. Conclusions

In recent decades, study of the UHI has become a field of research of great importance, motivated by a need to know which factors alter urban climates, so as to establish mitigation measures for future urban planning proposals.

In the present study, both the Sentinel day and Sentinel night UHI of the city of Granada were analyzed in view of the LCZ. This classification, based on characteristics of the landscape, is intended to determine the precise parameters that affect the UHI. Six LCZs were identified, and for each of them the variables that play an important role in increasing or decreasing the intensity of the UHI were determined and analyzed. We relied on Sentinel 3A (day) and 3B (night) satellite images, which afford the advantage of providing LST images over the city at a time interval of 10 h. By determining first the LST and then the UHI during the day and at night, we arrived at more specific results than traditional studies working with a single satellite image per day. The methodology used in this research, together with the morphological, geographical and pollution characteristics of the city, lend particular interest to the results obtained.

It may be concluded that the official Sentinel 3 products give higher LSTs than the ones obtained in situ using temperature probes. However, they show high precision and low sensitivity, and work well on a global scale even under high pollution conditions. They can thus be considered adequate to estimate the LST and UHI of a medium-sized city like Granada. Still, further applied research is needed to validate the accuracy of these products.

Our results detect higher mean LSTs in high-density areas of Granada than in low-density areas during the daytime. At night, LST readings are highest in compact areas, while open areas have lower temperatures.

The existence of seasonal variability of the UHI throughout the year has been corroborated. The highest intensity obtained with Sentinel day occurred in spring and with Sentinel night in autumn. The mean UHI obtained with Sentinel day throughout the study period shows negative values, whereas the mean UHI obtained with Sentinel night shows positive values. This suggests that during the morning the city is cooler than the surrounding rural areas, a phenomenon known as the urban cooling island. At dusk, the city is warmer than the neighboring rural areas, hence an urban heat island. It is interesting to note that a group of common factors affect both the day and night UHI of the city, while other factors affect just one time of the day.

Within the scope of each LCZ established, our findings were similar to those described globally for the city. Still, each area presents somewhat different intensities of daytime and nighttime UHI and conditioning factors. In terms of day UHI, higher negative intensities occur in the low-density areas, while high-density areas have lower negative intensities. Contrariwise, the highest intensities in the nocturnal UHI are produced in compact areas, not in open areas. Certain common factors affect both daytime and nighttime UHI; other factors are found to affect just one time of the day for each LCZ.

In the field of practice, the findings of this research stand as new knowledge about the UHI and its geographical and seasonal variability in the medium-sized and highly polluted city of Granada, which can be extrapolated to other cities in Europe and beyond. The use of six LCZs considered as standard in previous investigations allows us to compare the results obtained here with other investigations sharing this study base. Having free, easy access to two daily satellite images enhances the value of the methodology applied, making it suitable for future LST and UHI investigations in other cities.

At present, urban planners in charge of remodeling current urban areas and areas for future growth seek guidelines or criteria that will allow for sustainable development and that can be implemented gradually. This research and its results should prove useful for decision-making about plans and designs for land occupation, spatial distribution, urban density, energy, and public space, in efforts to dissipate pollution, reduce ambient temperature, improve energy savings in homes and public spaces, and increase thermal comfort for a given LCZ. The positive and negative temperatures determined within the city as opposed to rural areas may serve as a reference for

future research into efficient heating and air conditioning, or new sources with lower carbon emissions. After the relevant adequacy and effectiveness studies, such results could be extrapolated to other European cities.

6. Study limitations

The contributions of this article should be viewed, however, in light of certain limitations that justify the development of future research. Established as a priority is the possibility of recording measurements of greater duration (2–3 years) and with a greater number of images, to set more precise annual mean values and identify possible oscillations of UIH in the different seasons of the year. This might improve the effectiveness of measures implemented to mitigate the UHI phenomenon.

Author statement

All persons who meet authorship criteria are listed as authors, and all authors certify that they have participated sufficiently in the work to take public responsibility for the content, including participation in the concept, design, analysis, writing, or revision of the manuscript. Furthermore, each author certifies that this material or similar material has not been and will not be submitted to or published in any other publication before its appearance in the Urban Climate.

Declaration of Competing Interest

None.

References

- Alavipanah, S., Schreyer, J., Haase, D., Lakes, T., Qureshi, S., 2018. The effect of multi-dimensional indicators on urban thermal conditions. *J. Clean. Prod.* 177, 115–123. <https://doi.org/10.1016/j.jclepro.2017.12.187>.
- Alcock, I., White, M.P., Lovell, R., Higgins, S.L., Osborne, N.J., Husk, K., Wheeler, B.W., 2015. What accounts for “England’s green and pleasant land”? A panel data analysis of mental health and land cover types in rural England. *Landscape. Urban Plan.* 142, 38–46. <https://doi.org/10.1016/j.landurbplan.2015.05.008>.
- Anjos, M., Crésø, A., Krecl, P., Yoshikazu, G., Favaro, R., 2020. Analysis of the urban heat island under different synoptic patterns using local climate zones. *Build. Environ.* 185, 107268. <https://doi.org/10.1016/j.buildenv.2020.107268>.
- Arbuthnott, K.G., Hajat, S., 2017. The health effects of hotter summers and heat waves in the population of the United Kingdom: a review of the evidence. *Environmental Health: A Global Access Science Source* 16 (Suppl. 1), 1–13. <https://doi.org/10.1186/s12940-017-0322-5>.
- Arellano, B., Roca, J., Biere, R., 2018. Planning and urban climate: the example of the metropolitan area of Barcelona. In: *A: International Symposium on Remote Sensing, "SPIE Remote Sensing 2018"*. Washington: International Society for Photo-Optical Instrumentation Engineers (SPIE), pp. 1–17.
- Arnfield, A.J., 2003. Two decades of urban climate research: a review of turbulence, exchanges of energy and water, and the urban heat island. *Int. J. Climatol.* 23 (1), 1–26. <https://doi.org/10.1002/joc.859>.
- Barbieri, T., Despini, F., Teggi, S., 2018. A multi-temporal analyses of land surface temperature using Landsat-8 data and open source software: the case study of Modena, Italy. *Sustainability (Switzerland)* 10 (5). <https://doi.org/10.3390/su10051678>.
- Bereitschaft, B., Debbage, K., 2013. Urban form, air pollution, and CO₂ emissions in large U.S. metropolitan areas. *Prof. Geogr.* 65 (4), 612–635. <https://doi.org/10.1080/00330124.2013.799991>.
- Bremer, M., Mayr, A., Wichmann, V., Schmidner, K., Rutzinger, M., 2016. A new multi-scale 3D-GIS-approach for the assessment and dissemination of solar income of digital city models. *Comput. Environ. Urban Syst.* 57, 144–154. <https://doi.org/10.1016/j.compenvurbsys.2016.02.007>.
- Brousse, O., Georganos, S., Demuzere, M., Vanhuyse, S., Wouters, H., Wolff, E., Linard, C., van Lipzig, N.P.M., Dujardin, S., 2019. Using local climate zones in sub-Saharan Africa to tackle urban health issues. *Urban Clim.* 27 (December 2018), 227–242. <https://doi.org/10.1016/j.uclim.2018.12.004>.
- Carvalho, D., Martins, H., Marta-Almeida, M., Rocha, A., Borrego, C., 2017. Urban resilience to future urban heat waves under a climate change scenario: a case study for Porto urban area (Portugal). *Urban Clim.* 19, 1–27. <https://doi.org/10.1016/j.uclim.2016.11.005>.
- Ceplová, N., Kalusová, V., Lososová, Z., 2017. Effects of settlement size, urban heat island and habitat type on urban plant biodiversity. *Landscape. Urban Plan.* 159, 15–22. <https://doi.org/10.1016/j.landurbplan.2016.11.004>.
- Chen, Y., Li, X., Zheng, Y., Guan, Y., Liu, X., 2011. Estimating the relationship between urban forms and energy consumption: a case study in the Pearl River Delta, 2005–2008. *Landscape. Urban Plan.* 102 (1), 33–42. <https://doi.org/10.1016/j.landurbplan.2011.03.007>.
- Chiang, S., Ivan, N., 2020. Mapping and tracking Forest burnt areas in the Indio Maiz biological reserve using Sentinel-3 SLSTR and VIIRS-DNB imagery. *Sensors (Switzerland)* 19 (2019). <https://www.globalwildlife.org/project/indio-maiz-biological-reserve/>.
- Chun, B., Guldmann, J.M., 2014. Spatial statistical analysis and simulation of the urban heat island in high-density central cities. *Landscape. Urban Plan.* 125, 76–88. <https://doi.org/10.1016/j.landurbplan.2014.01.016>.
- Connors, J., Galletti, C., 2013. Landscape configuration and urban heat island effects: assessing the relationship between landscape characteristics and land surface temperature in Phoenix, Arizona. *Landscape. Ecol.* 28 (2), 271–283. <https://doi.org/10.1007/s10980-012-9833-1>.
- Conrad, O., Bechtel, B., Bock, M., Dietrich, H., Fischer, E., Gerlitz, L., Wehberg, J., Wichmann, V., Böhner, J., 2015. System for automated Geoscientific analyses (SAGA) v. 2.1.4. *Geoscientific Model Development Discussions* 8 (2), 2271–2312. <https://doi.org/10.5194/gmd-8-2271-2015>.
- Coppo, P., Ricciarelli, B., Brandani, F., Delderfield, J., Ferlet, M., Mutlow, C., Munro, G., Nightingale, T., Smith, D., Bianchi, S., Nicol, P., Kirschstein, S., Hennig, T., Engel, W., Frerick, J., Nieke, J., 2010. SLSTR: a high accuracy dual scan temperature radiometer for sea and land surface monitoring from space. *J. Mod. Opt.* 57 (18), 1815–1830. <https://doi.org/10.1080/09500340.2010.503010>.
- Cramer, W., Guiot, J., Fader, M., Garrabou, J., Gattuso, J.P., Iglesias, A., Lange, M.A., Lionello, P., Llasat, M.C., Paz, S., Peñuelas, J., Snoussi, M., Toreti, A., Tsimplis, M.N., Xoplaki, E., 2018. Climate change and interconnected risks to sustainable development in the Mediterranean. *Nat. Clim. Chang.* 8, 972–980. <https://doi.org/10.1038/s41558-018-0299-2>.
- Dai, Z., Guldmann, J.M., Hu, Y., 2018. Spatial regression models of park and land-use impacts on the urban heat island in Central Beijing. *Sci. Total Environ.* 626, 1136–1147. <https://doi.org/10.1016/j.scitotenv.2018.01.165>.
- De Castro, M., Gallardo, C., Jylha, K., Tuomenvirta, H., 2007. The use of a climate-type classification for assessing climate change effects in Europe from an ensemble of nine regional climate models. *Clim. Chang.* 81 (Suppl. 1), 329–341. <https://doi.org/10.1007/s10584-006-9224-1>.
- Diallo, J., Lacaze, B., Comby, J., 2015. Land surface temperature in the urban area of Lyon metropolis: a comparative study of remote sensing data and MesoNH model simulation. In: 2015 Joint Urban Remote Sensing Event, JURSE 2015, pp. 2–5. <https://doi.org/10.1109/JURSE.2015.7120528>.
- Dirksen, M., Ronda, R.J., Theeuwes, N.E., Pagani, G.A., 2019. Sky view factor calculations and its application in urban heat island studies. *Urban Clim.* 30 (May), 100498. <https://doi.org/10.1016/j.uclim.2019.100498>.

- Du, H., Cai, W., Xu, Y., Wang, Z., Wang, Y., Cai, Y., 2017. Quantifying the cool island effects of urban green spaces using remote sensing data. *Urban For. Urban Green.* 27, 24–31. <https://doi.org/10.1016/j.ufug.2017.06.008>.
- Du, J., Xiang, X., Zhao, B., Zhou, H., 2020. Impact of urban expansion on land surface temperature in Fuzhou, China using Landsat imagery. *Sustain. Cities Soc.* 61 (June), 102346. <https://doi.org/10.1016/j.scs.2020.102346>.
- Dwivedi, A., Mohan, B.K., 2018. Impact of green roof on micro climate to reduce urban Heat Island. *Remote Sensing Applications: Society and Environment* 10, 56–69. <https://doi.org/10.1016/j.rsase.2018.01.003>.
- Emmanuel, R., Krüger, E., 2012. *Urban heat island and its impact climate change resilience in a shrinking city: the case of Glasgow, UK.* *Build. Environ.* 53, 137–149.
- Equerre, V., Mirzaei, P.A., Riffat, S., 2020. Definition of a new morphological parameter to improve prediction of urban heat island. *Sustain. Cities Soc.* 56 (November 2019) <https://doi.org/10.1016/j.scs.2020.102021>.
- Estoque, R., Murayama, Y., Myint, S., 2017. Effects of landscape composition and pattern on land surface temperature: an urban heat island study in the megacities of Southeast Asia. *Sci. Total Environ.* 577, 349–359. <https://doi.org/10.1016/j.scitotenv.2016.10.195>.
- Fang, L., Tian, C., 2020. Construction land quotas as a tool for managing urban expansion. *Landscape. Urban Plan.* 195 (May 2019), 103727. <https://doi.org/10.1016/j.landurbplan.2019.103727>.
- Feizizadeh, B., Blaschke, T., 2013. Examining urban heat island relations to land use and air pollution: multiple endmember spectral mixture analysis for thermal remote sensing. *IEEE Journal of Selected Topics in Applied Earth Observations and Remote Sensing* 6 (3), 1749–1756. <https://doi.org/10.1109/JSTARS.2013.2263425>.
- Freeborn, P., Wooster, M., Roberts, G., Malamud, B., Xu, W., 2009. Development of a virtual active fire product for Africa through a synthesis of geostationary and polar orbiting satellite data. *Remote Sens. Environ.* 113, 1700–1711. <https://doi.org/10.1016/j.rse.2009.03.013>.
- Fu, P., Weng, Q., 2018. Variability in annual temperature cycle in the urban areas of the United States as revealed by MODIS imagery. *ISPRS J. Photogrammetry Remote Sens.* 146, 65–73. <https://doi.org/10.1016/j.isprsjprs.2018.09.003>.
- Garcia, V., Cuxart, J., Martínez, D., Jimenez, M.A., Simó, G., 2018. Comparison of three methods for estimating land surface temperature from Landsat 8-TIRS sensor data. *Remote Sens.* 10 (9), 1–13. <https://doi.org/10.3390/rs10091450>.
- Gaur, A., Eichenbaum, M.K., Simonovic, S.P., 2018. Analysis and modelling of surface urban Heat Island in 20 Canadian cities under climate and land-cover change. *J. Environ. Manag.* 206, 145–157. <https://doi.org/10.1016/j.jenvman.2017.10.002>.
- Guo, A., Yang, J., Xiao, X., Xia, J., Jin, C., Li, X., 2020. Influences of urban spatial form on urban heat island effects at the community level in China. *Sustain. Cities Soc.* 53, 101972. <https://doi.org/10.1016/j.scs.2019.101972>.
- Haashemi, S., Weng, Q., Darvishi, A., Alavipanah, K.S., 2016. Seasonal variations of the surface urban heat island in a semi-arid city. *Remote Sens.* 8 (4), 352. <https://doi.org/10.3390/rs8040352>.
- Häntzschel, J., Goldberg, V., Bernhofer, C., 2007. GIS-based regionalisation of radiation, temperature and coupling measures in complex terrain for low mountain ranges. *Meteorological Applications* 12, 33–42. <https://doi.org/10.1017/S1350482705001489>.
- Hu, Y., Dai, Z., Guldmann, J.M., 2020. Modeling the impact of 2D/3D urban indicators on the urban heat island over different seasons: a boosted regression tree approach. *J. Environ. Manag.* 266 (11), 110424. <https://doi.org/10.1016/j.jenvman.2020.110424>.
- Hua, L., Zhang, X., Nie, Q., Sun, F., Tang, L., 2020. The impacts of the expansion of urban impervious surfaces on urban heat islands in a coastal city in China. *Sustainability (Switzerland)* 12 (2). <https://doi.org/10.3390/su12020475>.
- Jato, D., 2019. Spatiotemporal statistical analysis of the Urban Heat Island effect in a Mediterranean region. *Sustain. Cities Soc.* 46 (January), 101427. <https://doi.org/10.1016/j.scs.2019.101427>.
- Karakus, C.B., 2019. The impact of land use/land cover (LULC) changes on land surface temperature in Sivas City Center and its surroundings and assessment of urban Heat Island. *Asia-Pac. J. Atmos. Sci.* 55 (4), 669–684. <https://doi.org/10.1007/s13143-019-00109-w>.
- Keramitsoglou, I., Kiranoudis, C.T., Ceriola, G., Weng, Q., Rajasekar, U., 2011. Identification and analysis of urban surface temperature patterns in greater Athens, Greece, using MODIS imagery. *Remote Sens. Environ.* 115 (12), 3080–3090. <https://doi.org/10.1016/j.rse.2011.06.014>.
- Khamchiangta, D., Dhakal, S., 2019. Physical and non-physical factors driving urban heat island: case of Bangkok metropolitan administration, Thailand. *J. Environ. Manag.* 248 (July), 109285. <https://doi.org/10.1016/j.jenvman.2019.109285>.
- Kim, J.J., Kim, D.Y., 2009. Effects of a building's density on flow in urban areas. *Adv. Atmos. Sci.* 26 (1), 45–56. <https://doi.org/10.1007/s00376-009-0045-9>.
- Kovats, R.S., Campbell, D., Matthies, F., 2005. Climate change and human health: estimating avoidable deaths and disease. *Risk Anal.* 25 (6), 1409–1418. <https://doi.org/10.1111/j.1539-6924.2005.00688.x>.
- Labra, R., 2014. Zero panel data guide. (Cátedra UA). file:///U:/Maguilera/Documentos Personales MAGUILERA/Master M3F/Trabajo Fin M3F/Revisión para paper/Referencias/Stata/16_Guia CERO para datos de panel.Un enfoque practico.pdf.
- Lemus, M., Martin, J., Moreno, M.C., Lopez, J.A., 2020. Estimating Barcelona's metropolitan daytime hot and cold poles using Landsat-8 land surface temperature. *Sci. Total Environ.* 699, 134307. <https://doi.org/10.1016/j.scitotenv.2019.134307>.
- Li, T., Meng, Q., 2018. A mixture emissivity analysis method for urban land surface temperature retrieval from Landsat 8 data. *Landscape. Urban Plan.* 179 (July), 63–71. <https://doi.org/10.1016/j.landurbplan.2018.07.010>.
- Li, X., Zhou, W., 2019. Spatial patterns and driving factors of surface urban heat island intensity: a comparative study for two agriculture-dominated regions in China and the USA. *Sustain. Cities Soc.* 48, 101518. <https://doi.org/10.1016/j.scs.2019.101518>.
- Li, J., Song, C., Cao, L., Zhu, F., Meng, X., Wu, J., 2011. Impacts of landscape structure on surface urban heat islands: a case study of Shanghai, China. *Remote Sens. Environ.* 115 (12), 3249–3263. <https://doi.org/10.1016/j.rse.2011.07.008>.
- Lin, W., Ting, Y., Chang, X., Wu, W., Zhang, Y., 2015. Calculating cooling extents of green parks using remote sensing: method and test. *Landscape. Urban Plan.* 134, 66–75. <https://doi.org/10.1016/j.landurbplan.2014.10.012>.
- Logan, T.M., Zaitchik, B., Guikema, S., Nisbet, A., 2020. Night and day: the influence and relative importance of urban characteristics on remotely sensed land surface temperature. *Remote Sens. Environ.* 247, 111861. <https://doi.org/10.1016/j.rse.2020.111861>.
- MacIntyre, H.L., Heaviside, C., Taylor, J., Picetti, R., Symonds, P., Cai, X.M., Vardoulakis, S., 2018. Assessing urban population vulnerability and environmental risks across an urban area during heatwaves – implications for health protection. *Sci. Total Environ.* 678–690. <https://doi.org/10.1016/j.scitotenv.2017.08.062>.
- Mallick, J., Rahman, A., Singh, C.K., 2013. Modeling urban heat islands in heterogeneous land surface and its correlation with impervious surface area by using nighttime ASTER satellite data in highly urbanizing city, Delhi-India. *Adv. Space Res.* 52 (4), 639–655. <https://doi.org/10.1016/j.asr.2013.04.025>.
- Masoudi, M., Yok, P., Fadaei, M., 2021. The effects of land use on spatial pattern of urban green spaces and their cooling ability. *Urban Clim.* 35, 100743. <https://doi.org/10.1016/j.ulclim.2020.100743>.
- McMillin, L.M., 1975. Estimation of sea surface temperatures from two infrared window measurements with different absorption. *J. Geophys. Res.* 80 (36), 5113–5117. <https://doi.org/10.1029/jc080i036p05113>.
- Meng, X., Cheng, J., Zhao, S., Liu, S., Yao, Y., 2019. Estimating land surface temperature from Landsat-8 data using the NOAA JPSS enterprise algorithm. *Remote Sens.* 11 (2) <https://doi.org/10.3390/rs11020155>.
- Mukherjee, F., Singh, D., 2020. Assessing land use-land cover change and its impact on land surface temperature using LANDSAT data: a comparison of two urban areas in India. *Earth Systems and Environment* 4 (2), 385–407. <https://doi.org/10.1007/s41748-020-00155-9>.
- Oke, T.R., 1987. *Boundary Layer Climates* (Routledge).
- Olaya, V., Conrad, O., 2009. Geomorphometry in SAGA. *Dev. Soil Sci.* 33 (C), 293–308. [https://doi.org/10.1016/S0166-2481\(08\)00012-3](https://doi.org/10.1016/S0166-2481(08)00012-3).
- Oliveira, A., Lopes, A., Niza, S., 2020. Local climate zones in five southern European cities: an improved GIS-based classification method based on Copernicus data. *Urban Clim.* 33 (May 2019), 100631. <https://doi.org/10.1016/j.ulclim.2020.100631>.
- ONU, 2018. 68% of the world population projected to live in urban areas by 2050, says UN. <https://www.un.org/development/desa/en/news/population/2018-revision-of-world-urbanization-prospects.html>.
- Peng, J., Jia, J., Liu, Y., Li, H., Wu, J., 2018. Seasonal contrast of the dominant factors for spatial distribution of land surface temperature in urban areas. *Remote Sensing Environment.* 215, 255–267. <https://doi.org/10.1016/j.rse.2018.06.010>.

- Priaziuk, E., Van der Tol, C., 2019. Global sensitivity analysis of the SCOPE model in Sentinel-3 bands: thermal domain focus. *Remote Sens.* 11 (20) <https://doi.org/10.3390/rs11202424>.
- Qiu, C., Schmitt, M., Mou, L., Ghamisi, P., Zhu, X.X., 2018. Feature importance analysis for local climate zone classification using a residual convolutional neural network with multi-source datasets. *Remote Sens.* 10, 1572. <https://doi.org/10.3390/rs10101572>.
- Ramamurthy, P., Bou-Zeid, E., 2017. Heatwaves and urban heat islands: a comparative analysis of multiple cities. *J. Geophys. Res.* 122, 168–178. <https://doi.org/10.1002/2016JD025357>.
- Rasilla, D., Allende, F., Martilli, A., Fernández, F., 2019. Heat waves and human well-being in Madrid (Spain). *Atmosphere*. 288 <https://doi.org/10.3390/atmos10050288>.
- Remedios, J., 2012. *Sentinel-3 optical products and algorithm definition land surface temperature*, 24.
- Romero, L., Sánchez, J., Sánchez, F.J., Álvarez, S., 2020. Analyzing the urban heat island: comprehensive methodology for data gathering and optimal design of mobile transects. *Sustain. Cities Soc.* 55 <https://doi.org/10.1016/j.scs.2020.102027>.
- Roy, S., Pandit, S., Eva, E.A., Bagmar, M.S.H., Papia, M., Banik, L., Dubé, T., Rahman, F., Razi, M.A., 2020. Examining the nexus between land surface temperature and urban growth in Chattogram metropolitan area of Bangladesh using long term Landsat series data. *Urban Clim.* 32 (January), 100593. <https://doi.org/10.1016/j.ulclim.2020.100593>.
- Rozos, E., Makropoulos, C., Maksimović, Č., 2013. Rethinking urban areas: an example of an integrated blue-green approach. *Water Sci. Technol. Water Supply* 13 (6), 1534–1542. <https://doi.org/10.2166/ws.2013.140>.
- Ruescas, A.B., Danne, O., Fomferra, N., Brockmann, C., 2016. The land surface temperature synergistic processor in beam: a prototype towards sentinel-3. *Data* 1 (3), 1–14. <https://doi.org/10.3390/data1030018>.
- Rui, Y., Wang, L., Huang, X., Zhang, W., Li, J., Niu, Z., 2018. Interannual variations in surface urban heat island and associated drivers in China. *J. Environ. Manag.* 222, 86–94. <https://doi.org/10.1016/j.jenvman.2018.05.024>.
- Saaroni, H., Amorim, J.H., Hiemstra, J.A., Pearlmuter, D., 2018. Urban green infrastructure as a tool for urban heat mitigation: survey of research methodologies and findings across different climatic regions. *Urban Clim.* 24 (October 2017), 94–110. <https://doi.org/10.1016/j.ulclim.2018.02.001>.
- Santamouris, M., 2020. Recent progress on urban overheating and heat island research. Integrated assessment of the energy, environmental, vulnerability and health impact. Synergies with the global climate change. *Energy and Buildings* 207. <https://doi.org/10.1016/j.enbuild.2019.109482>.
- Sarrat, C., Lemonsu, A., Masson, V., Guedalia, D., 2006. Impact of urban heat island on regional atmospheric pollution. *Atmos. Environ.* 40 (10), 1743–1758. <https://doi.org/10.1016/j.atmosenv.2005.11.037>.
- Schneider, A., Friedl, M.A., Potere, D., 2010. Mapping global urban areas using MODIS 500-m data: New methods and datasets based on “urban ecoregions”. *Remote Sens. Environ.* 114 (8), 1733–1746. <https://doi.org/10.1016/j.rse.2010.03.003>.
- Schwarz, N., Lautenbach, S., Seppelt, R., 2011. Exploring indicators for quantifying surface urban heat islands of European cities with MODIS land surface temperatures. *Remote Sens. Environ.* 115, 3175–3186. <https://doi.org/10.1016/j.rse.2011.07.003>.
- Sclozzari, R., Genetelli, D., 2012. A multi-scale qualitative approach to assess the impact of urbanization on natural habitats and their connectivity. *Environ. Impact Assess. Rev.* 36, 9–22. <https://doi.org/10.1016/j.eiar.2012.03.001>.
- Sejati, A.W., Buchori, I., Rudiarto, I., 2019. The spatio-temporal trends of urban growth and surface urban heat islands over two decades in the Semarang metropolitan region. *Sustain. Cities Soc.* 46 (January), 101432. <https://doi.org/10.1016/j.scs.2019.101432>.
- Sekertekin, A., 2019. Validation of physical Radiative transfer equation-based land surface temperature using Landsat 8 satellite imagery and SURFRAD in-situ measurements. *J. Atmos. Sol. Terr. Phys.* 196 (July), 105161. <https://doi.org/10.1016/j.jastp.2019.105161>.
- Sekertekin, A., Bonafoni, S., 2020. Land surface temperature retrieval from Landsat 5, 7, and 8 over rural areas: assessment of different retrieval algorithms and emissivity models and toolbox implementation. *Remote Sens.* 12 (2) <https://doi.org/10.3390/rs12020294>.
- Seto, K.C., Kaufmann, R.K., 2003. Modeling the drivers of urban land use change in the Pearl River Delta, China: integrating remote sensing with socioeconomic data. *Land Econ.* 79 (1), 106–121. <https://doi.org/10.2307/3147108>.
- Shafizadeh, H., Weng, Q., Liu, H., Valavi, R., 2020. Modeling the spatial variation of urban land surface temperature in relation to environmental and anthropogenic factors: a case study of Tehran, Iran. *GIScience and Remote Sensing* 57 (4), 483–496. <https://doi.org/10.1080/15481603.2020.1736857>.
- Smith, R.J., Hsiao, C., 1988. Analysis of panel data. *Economica* 55 (218), 284. <https://doi.org/10.2307/2554479>.
- Sobrino, J.A., Jiménez, J.C., Sòria, G., Ruescas, A.B., Danne, O., Brockmann, C., Ghent, D., Remedios, J., North, P., Merchant, C., Berger, M., Mathieu, P.P., Götsche, F.M., 2016. Synergistic use of MERIS and AATSR as a proxy for estimating Land Surface Temperature from Sentinel-3 data. *Remote Sens. Environ.* 179, 149–161. <https://doi.org/10.1016/j.rse.2016.03.035>.
- Son, N.T., Chen, C.F., Chen, C.R., Thanh, B.X., Vuong, T.H., 2017. Assessment of urbanization and urban heat islands in Ho Chi Minh City, Vietnam using Landsat data. *Sustain. Cities Soc.* 30, 150–161. <https://doi.org/10.1016/j.scs.2017.01.009>.
- Song, J., Lin, T., Li, X., Prishchepov, A.V., 2018. Mapping urban functional zones by integrating very high spatial resolution remote sensing imagery and points of interest: a case study of Xiamen, China. *Remote Sens.* 10 (11) <https://doi.org/10.3390/rs10111737>.
- Song, J., Chen, W., Zhang, J., Huang, K., Hou, B., Prishchepov, A.V., 2020. Effects of building density on land surface temperature in China: spatial patterns and determinants. *Landscape Urban Plan.* 198 (March), 103794. <https://doi.org/10.1016/j.landurbplan.2020.103794>.
- Soydan, O., 2020. Effects of landscape composition and patterns on land surface temperature: urban heat island case study for Nigde, Turkey. *Urban Clim.* 34, 100688. <https://doi.org/10.1016/j.ulclim.2020.100688>.
- Srivastava, P.K., Majumdar, T.J., Bhattacharya, A.K., 2009. Surface temperature estimation in Singhbhum shear zone of India using Landsat-7 ETM+ thermal infrared data. *Adv. Space Res.* 43 (10), 1563–1574. <https://doi.org/10.1016/j.asr.2009.01.023>.
- Stewart, I.D., 2011. A systematic review and scientific critique of methodology in modern urban heat island literature. *Int. J. Climatol.* 31 (2), 200–217. <https://doi.org/10.1002/joc.2141>.
- Stewart, I., Oke, T., 2009. Classifying urban climate field sites by “local climate zones”: The case of Nagano, Japan. In: *The Seventh International Conference on Urban Climate, July*, pp. 1–5.
- Stewart, I.D., Oke, T., 2012. Local climate zones for urban temperature studies. *Bull. Am. Meteorol. Soc.* 93 (12), 1879–1900. <https://doi.org/10.1175/BAMS-D-11-00019.1>.
- Straub, A., Berger, K., Breitner, S., Cyrys, J., Geruschkat, U., Jacobbeit, J., Kühlbach, B., Kusch, T., Philipp, A., Schneider, A., Umminger, R., Wolf, K., Beck, C., 2019. Statistical modelling of spatial patterns of the urban heat island intensivitiy in the urban environment of Augsburg, Germany. *Urban Clim.* 29, 100491. <https://doi.org/10.1016/j.ulclim.2019.100491>.
- Sun, H., Gui, D., Yan, B., Liu, Y., Liao, W., Zhu, Y., Lu, C., Zhao, N., 2016. Assessing the potential of random forest method for estimating solar radiation using air pollution index. *Energy Convers. Manag.* 119, 121–129. <https://doi.org/10.1016/j.enconman.2016.04.051>.
- Tan, M., Li, X., 2015. Quantifying the effects of settlement size on urban heat islands in fairly uniform geographic areas. *Habitat International* 49, 100–106. <https://doi.org/10.1016/j.habitatint.2015.05.013>.
- Tsou, J., Zhuang, J., Li, Y., Zhang, Y., 2017. Urban Heat Island assessment using the Landsat 8 data: a case study in Shenzhen and Hong Kong. *Urban Sci.* 1 (1), 10. <https://doi.org/10.3390/urbansci1010010>.
- Van Hove, L.W.A., Jacobs, C.M.J., Heusinkveld, B.G., Elbers, J.A., Van Driel, B.L., Holtslag, A.A.M., 2015. Temporal and spatial variability of urban heat island and thermal comfort within the Rotterdam agglomeration. *Build. Environ.* 83, 91–103. <https://doi.org/10.1016/j.buildenv.2014.08.029>.
- Venter, Z., Brousse, O., Esau, I., Meier, F., 2020. Hyperlocal mapping of urban air temperature using remote sensing and crowdsourced weather data. *Remote Sens. Environ.* 242, 111791. <https://doi.org/10.1016/j.rse.2020.111791>.
- Walawender, J.P., Szymanowski, M., Hajto, M.J., Bokwa, A., 2014. Land surface temperature patterns in the urban agglomeration of Krakow (Poland) derived from Landsat-7/ETM+ data. *Pure Appl. Geophys.* 171 (6), 913–940. <https://doi.org/10.1007/s0024-013-0685-7>.
- Wan, Z., 2013. New refinements and validation of the collection-6 MODIS land-surface temperature/emissivity product. *Remote Sens. Environ.* 140, 36–45. <https://doi.org/10.1016/j.rse.2013.08.027>.

- Wang, J., Ouyang, W., 2017. Attenuating the surface urban Heat Island within the local thermal zones through land surface modification. *J. Environ. Manag.* 187, 239–252. <https://doi.org/10.1016/j.jenvman.2016.11.059>.
- Wang, M., Madden, M., Liu, X., 2017. Exploring the relationship between urban forms and CO₂ emissions in 104 Chinese cities. *Journal of Urban Planning and Development* 143 (4), 1–8. [https://doi.org/10.1061/\(ASCE\)UP.1943-5444.0000400](https://doi.org/10.1061/(ASCE)UP.1943-5444.0000400).
- Wang, L., Lu, Y., Yao, Y., 2019. Comparison of three algorithms for the retrieval of land surface temperature from landsat 8 images. *Sensors (Switzerland)* 19 (22). <https://doi.org/10.3390/s19225049>.
- Ward, K., Lauf, S., Kleinschmit, B., Endlicher, W., 2016. Heat waves and urban heat islands in Europe: a review of relevant drivers. *Sci. Total Environ.* 569–570, 527–539. <https://doi.org/10.1016/j.scitotenv.2016.06.119>.
- Wooster, M.J., Xu, W., Nightingale, T., 2012. Sentinel-3 SLSTR active fire detection and FRP product: pre-launch algorithm development and performance evaluation using MODIS and ASTER datasets. *Remote Sensing Environment* 120, 236–254. <https://doi.org/10.1016/j.rse.2011.09.033>.
- Wu, C., Li, J., Wang, C., Song, C., Chen, Y., Finka, M., La Rosa, D., 2019. Understanding the relationship between urban blue infrastructure and land surface temperature. *Sci. Total Environ.* 694 <https://doi.org/10.1016/j.scitotenv.2019.133742>.
- Xiao, H., Weng, Q., 2007. The impact of land use and land cover changes on land surface temperature in a karst area of China. *J. Environ. Manag.* 85, 245–257. <https://doi.org/10.1016/j.jenvman.2006.07.016>.
- Xu, W., Wooster, M., He, J., Zhang, T., 2020. First study of Sentinel-3 SLSTR active fire detection and FRP retrieval: nighttime algorithm enhancements and global intercomparison to MODIS and VIIRS AF products. *Remote Sens. of Environ.* 248, 111947. <https://doi.org/10.1016/j.rse.2020.111947>.
- Yang, C., Wang, R., Zhang, S., Ji, C., Fu, X., 2019. Characterizing the hourly variation of urban heat islands in a snowy climate city during summer. *Int. J. Environ. Res. Public Health* 16 (14). <https://doi.org/10.3390/ijerph16142467>.
- Yang, C., Yan, F., Zhang, S., 2020a. Comparison of land surface and air temperatures for quantifying summer and winter urban heat island in a snow climate city. *J. Environ. Manag.* 265 (March), 110563. <https://doi.org/10.1016/j.jenvman.2020.110563>.
- Yang, J., Zhou, J., Götsche, F.-M., Long, Z., Ma, J., Luo, R., 2020b. Investigation and validation of algorithms for estimating land surface temperature from Sentinel-3 SLSTR data. *Int. J. Appl. Earth Obs. Geoinf.* 91 (April), 102136. <https://doi.org/10.1016/j.jag.2020.102136>.
- Yao, R., Wang, L., Huang, X., Zhang, W., Li, J., Niu, Z., 2018. Interannual variations in surface urban heat island intensity and associated drivers in China. *J. Environ. Manag.* 222 (April), 86–94. <https://doi.org/10.1016/j.jenvman.2018.05.024>.
- Yu, Z., Guo, X., Jørgensen, G., Vejre, H., 2017. How can ur-ban green spaces be planned for climate adaptation in subtropical cities? *Ecol. Indic.* 82, 152–162. <https://doi.org/10.1016/j.ecolind.2017.07.002>.
- Yue, W., 2013. Thermal environment effect of urban water landscape. *Hengtai Xuebao* 6 (10000933), 1852–1859. <https://doi.org/10.5846/%0Astxb201112141915>.
- Zakšek, K., Podobnikar, T., Oštir, K., 2005. Solar radiation modelling. *Comput. Geosci.* 31 (2), 233–240. <https://doi.org/10.1016/j.cageo.2004.09.018>.
- Zhao, L., Oppenheimer, M., Zhu, Q., Baldwin, J.W., Ebi, K.L., Bou-Zeid, E., Guan, K., Liu, X., 2018. Interactions between urban heat islands and heat waves. *Environ. Res. Lett.* 13 <https://doi.org/10.1088/1748-9326/aa9f73>.
- Zhou, D., Zhao, S., Liu, S., Zhang, L., Zhu, C., 2014. Remote sensing of environment surface urban heat island in China's 32 major cities: spatial patterns and drivers. *Remote Sens. Environ.* 152, 51–61. <https://doi.org/10.1016/j.rse.2014.05.017>.
- Zhou, C., Li, S., Wang, S., 2018. Examining the impacts of urban form on air pollution in developing countries: a case study of China's megacities. *Int. J. Environ. Res. Public Health* 15 (8). <https://doi.org/10.3390/ijerph15081565>.